BRNO UNIVERSITY OF TECHNOLOGY

VYSOKÉ UČENÍ TECHNICKÉ V BRNĚ

FACULTY OF MECHANICAL ENGINEERING

FAKULTA STROJNÍHO INŽENÝRSTVÍ

INSTITUTE OF PHYSICAL ENGINEERING

ÚSTAV FYZIKÁLNÍHO INŽENÝRSTVÍ

FREQUENCY-SWEPT RAPID-SCAN EPR ON ORGANIC RADICALS

FREKVENČNÍ RAPID-SCAN EPR NA ORGANICKÝCH RADIKÁLECH

MASTER'S THESIS

DIPLOMOVÁ PRÁCE

AUTHOR — **Bc. MAREK TUČEK**

AUTOR PRÁCE

SUPERVISOR — **Ing. PETR NEUGEBAUER, Ph.D.**

VEDOUCÍ PRÁCE

BRNO 2018

BRNO UNIVERSITY OF TECHNOLOGY
FACULTY OF MECHANICAL ENGINEERING

Specification Master's Thesis

Department:	Institute of Physical Engineering
Student:	**Bc. Marek Tuček**
Study programme:	Applied Sciences in Engineering
Study branch:	Physical Engineering and Nanotechnology
Leader:	**Ing. Petr Neugebauer, Ph.D.**
Academic year:	2017/18

Pursuant to Act no. 111/1998 concerning universities and the BUT study and examination rules, you have been assigned the following topic by the institute director Master's Thesis:

Frequency–swept rapid–scan EPR on organic radicals

Concise characteristic of the task:

Rapid–scan Electron Paramagnetic Resonance (EPR) is an innovative method of researching paramagnetic materials. With respect to conventional EPR techniques, the method uses rapid sweeps over resonance lines, which allow access to relaxation times. Today, the method uses magnetic field to create rapid sweeps over resonance at constant microwave frequency. This method depending on the sweep rate allows access to relaxation times of investigated species. However, the use of rapid magnetic field sweeps has a lot of limitations mainly caused by restricted sweep rates and amplitudes of the fast changing magnetic field as well as its implementation to strong magnetic fields and low temperatures. On the other side, frequency rapid scans at constant magnetic field do not suffer by these limitations.

Goals Master's Thesis:

1. Perform a research study of Rapid–Scan EPR and related techniques in order to set the theoretical base for the frequency rapid scan experiments.
2. Perform frequency rapid scan experiment on selected organic radicals.
3. Perform analysis of obtained data and draw conclusion out of the experiments.

Recommended bibliography:

HYDE, J.S. et al., W-band frequency-swept EPR, Journal of Magnetic Resonance 205 (2010) 93-101

TSEITLIN, M. et al., Rapid frequency scan EPR, Journal of Magnetic Resonance 211 (2011) 156-161

JOSHI, P.J. et al., Rapid-scan EPR with triangular scans and fourier deconvolution to recover the slow-scan spectrum, Journal of Magnetic Resonance 175 (2005) 44-51

DADOK, J., SPRECHER, R.F., Correlation NMR Spectroscopy, Journal of Magnetic Resonance 13 (1974) 243-248

GILBERT, B.C., DAVIES, M.J., MURPHY, D.M., ELECTRON PARAMAGNETIC RESONANCE vol.18, ISBN: 0-85404-315-2

WEIL, J.A., BOLTON, J.R., ELECTRON PARAMAGNETIC RESONANCE, 2007, ISBN: 978-047--75496-1

Deadline for submission Master's Thesis is given by the Schedule of the Academic year 2017/18

In Brno,

L. S.

prof. RNDr. Tomáš Šikola, CSc.
Director of the Institute

doc. Ing. Jaroslav Katolický, Ph.D.
FME dean

Abstract
This thesis describes a historically first multi-frequency rapid-scan EPR. While introducing microwave radiation at 200 GHz range with subsequent sinusoidal modulation, the frequency sweep rates up to 61 500 THz/s were achieved and the rapid passage distortion known as "wiggles" was observed in the spectra of both studied organic radicals samples – BDPA in a polystyrene matrix and LiPc. This thesis presents a flexible method of conducting rapid-scan EPR experiments, using a voltage controlled oscillator (VCO) and zero-bias detector (ZBD) as a source and detector, respectively, and thus opening the possibility to advance further into high field / high frequency range. Furthermore, the method of extracting the steady-state absorption spectra from the rapid-scan results, known as Fourier deconvolution, is described and subsequently, the spin dephasing times of the samples are determined from the comparison of the spectra with the results of numerically solved Bloch equations. The resulting values are 50 ns for BDPA and 12 ns for LiPc.

Abstrakt
Tato práce popisuje historicky první multi-frekvenční rapid-scan EPR. Při zavedení mikrovlnného záření z oblasti 200 GHz a následnou sinusovou modulací bylo dosaženo rychlostí změn frekvence až 61 500 THz/s a zkreslení spekter, známé jako "wiggles", bylo pozorováno u obou studovaných vzorků organických radikálů – BDPA v polystyrenové matici a LiPc. Tato práce představuje flexibilní metodu provádění rapid-scan EPR experimentů za použití napětím ovládaného oscilátoru (Voltage Controlled Oscillator; VCO) jako zdroje a zero-bias detektoru (ZBD) pro detekci, čímž se otevírá možnost postupu dále do oblastí vyšších polí / vyšších frekvencí. Dále je popsán postup získání ustáleného spektra z rapid-scan výsledků, známý jako Fourierovská dekonvoluce, a dále je zjistěn spinový dekoherenční čas vzorků pomocí srovnání experimentálních spekter s výsledky numericky vyřešených Blochových rovnic. Výsledné hodnoty jsou 50 ns pro BDPA a 12 ns pro LiPc.

Keywords
Frequency-swept rapid-scan EPR, wiggles, spin-spin relaxation time, Fourier deconvolution, Bloch equations

Klíčová slova
Frekvenční rapid-scan EPR, wiggles, spin-spin relaxační čas, Fourierovská dekonvoluce, Blochovy rovnice

TUČEK, M. *Frequency-swept rapid-scan EPR on organic radicals.* Brno University of Technology, Faculty of Mechanical Engineering, 2018. 59 p. Supervised by Ing. Petr Neugebauer, Ph.D.

I hereby confirm that my Master's Thesis: *Frequency-swept rapid scan EPR on organic radicals* was written by myself and myself only under the supervision of Ing. Petr Neugebauer, Ph.D. with the use of sources quoted in References.

Bc. Marek Tuček

I would like to thank everyone who directly or indirectly contributed to this project.
Special thanks belong to my supervisor Dr. Petr Neugebauer of CEITEC BUT and Dr. Oleksii Laguta of the University of Stuttgart, whose invaluable and endless help made this thesis possible. I would also like to thank Prof. Joris van Slageren of the University of Stuttgart, who accepted me into his group during my ERASMUS+ period, when this project began and then let me come over and over again to conduct experiment, and to Prof. Tomáš Šikola of the Institute of Physical Engineering, FME BUT. Also to my friends and colleagues from CEITEC BUT and the Institute of Physical Engineering.
This work was carried out with the support of CEITEC Nano Research Infrastructure (MEYS CR, 2016–2019).
This research has been financially supported by the Ministry of Education, Youth and Sports of the Czech Republic under the project CEITEC 2020 (LQ1601).
My eternal thanks goes to my lifelong friends for their love and support, David Pola and Jáchym Zeman, and my beautiful and kind wife, Tereza.
93.

Bc. Marek Tuček

Contents

1 Introduction

Much of the knowledge of the structure of molecules has been obtained from the analysis of molecular absorption spectra. Such spectra are obtained by measuring the attenuation versus frequency (or wavelength) of a beam of electromagnetic radiation as it passes through a sample of matter. Lines or bands in a spectrum represent transitions between energy levels of the absorbing species. The frequency of each line or band measures the energy separation of two levels.

When a photon is absorbed or emitted by an electron, atom or molecule, the energy and angular momentum of the combined (total) system must be conserved. For this reason, the propagation direction relative to the alignments of the photoactive chemical system is of crucial importance.

In most spectroscopic studies it is the electric field component of the electromagnetic radiation that interacts with molecules. However, a molecule containing a magnetic dipole might be expected to interact with the oscillating magnetic field component $\boldsymbol{B}_1$ – this forms the basis for magnetic resonance spectroscopy. A static magnetic field $\boldsymbol{B}_0$ is usually applied, in addition to $\boldsymbol{B}_1$, to align the moments and shift the energy levels to achieve conveniently measurable splitting. Each electron possesses an intrinsic magnetic dipole moment arising from spin. In most systems electrons occur in pairs such that the net moment is zero. Hence only species containing one or more unpaired electrons possess the net spin moment necessary for suitable interaction with an electromagnetic field. A magnetic dipole moment in an atom or molecule may arise from unpaired electrons as well as from magnetic nuclei. The magnetic dipole moment of these particles in turn arise, respectively, from electronic or nuclear angular momenta. Hence one of the fundamental phenomena to be understood in Electron Paramagnetic Resonance (EPR) spectroscopy is the nature and quantization of angular momenta.[1]

The technique of EPR spectroscopy may be regarded as a fascinating extension of the famous Stern-Gerlach experiment. In one of the fundamental experiments on the structure of matter, Stern and Gerlach[2] in the 1920s showed that electron magnetic moment in an atom can take on only discrete orientations in a magnetic field, despite the sphericity of the atom. Subsequently, Uhlenbeck and Goudsmit[3] linked the electron magnetic moment with the concept of electron spin angular momentum. In the hydrogen atom, one has additional angular momentum arising from the proton nucleus. Breit and Rabi[4] described the resultant energy levels of a hydrogen atom in a magnetic field in 1931. Rabi et al.[5] studied transitions between levels induced by an oscillating magnetic field. This experiment was the first observation of magnetic resonance.

The first observation of an electron paramagnetic resonance peak was made in 1945 when Zavoisky[6] detected a radiofrequency absorption line from a $CuCl_2 \cdot 2H_2O$ sample. He found a resonance at a magnetic field of 4.76 mT for a frequency of 133 MHz; in this case the electron Zeeman g-factor is approximately 2. Zavoisky's results were interpreted by Frenkel[7] as showing paramagnetic resonance absorption. Later experiments at higher (microwave) frequencies in magnetic field of 100-300 mT showed the advantages of the use of high frequencies and fields.[1]

Nowadays, EPR works mostly in two distinct regimes: (i) continuous wave (CW), where the microwave frequency is kept constant and the external magnetic field is slowly swept through the spectrum, and (ii) pulsed regime, where one or more short microwave pulses are administered to the sample while the magnetic field is kept constant. Both these regimes were highly perfected over time and are used in a variety of applications, including material and chemical research, spintronics, dosimetry and food industry. The rapid-scan regime, however, utilizes the strongest aspects of both conventional regimes while leaving behind some of the limiting factors.

In rapid-scan regime the resonance is passed through in a time that is short relative to the electron spin relaxation. This is done either by sweeping the magnetic field while the frequency is fixed or by sweeping the frequency while the field is fixed. Field-swept rapid-scan carries some intrinsic disadvantages – low sweep rates, eddy currents in the equipment and sample heating (thus the field-swept rapid-scan experiments are generally conducted at ambient temperature). On the contrary, frequency-swept rapid-scan, which has been enabled not a long time ago due to significant improvement in microwave technology, can achieve very high sweeping rates and avoids general problems caused by additional magnetic coils (as in field-swept).

The main strength of rapid-scan, as the name suggests, is the speed of data acquisition. Compared to CW experiments, where the data acquisition and averaging can take up to hours or days, the rapid-scan experiment is performed (with satisfying results) in a matter of milliseconds. Among another advantages is not requiring a high-power pulse source (which is currently extremely expensive for frequencies above 100 GHz) as with the pulsed techniques, as well as no need for a resonating cavity, therefore no strict requirement on the sample size; when using a resonant cavity, its size decreases with wavelength (at 10 GHz, $\lambda = 3$ cm, while at 300 GHz, $\lambda = 1$ mm). Minimal heating of the sample should also be mentioned.

To understand the origin of rapid-scan EPR, one must look back to discoveries made in Nuclear Magnetic Resonance (NMR), on which the rapid-scan EPR is built. Early in the development of NMR, transient effects, called "wiggles", were observed after the magnetic field passed through resonance in a time that was short relative to the relaxation times. Since inhomogeneity over the sample causes the oscillations to damp out more rapidly, this effect was used in continuous-wave NMR to guide the shimming of the magnetic field to maximum homogeneity. It was shown that the slow-scan NMR spectra could be recovered from rapid-scan signals by deconvolution or cross-correlation, using either a standard experimental response[8,9] or an analytic function[10–12]. It is worth mentioning that Prof. Dadok, a long time resident of Brno and a holder of an honorary doctorate of Brno University of Technology (2013), contributed invaluably to the development of NMR and its rapid-scan regime. Rapid-scan NMR achieved almost as high signal-to-noise ratio, per unit time, for proton spectra of simple organic molecules in fluid solution as could be achieved by pulsed Fourier-Transform NMR. However promising the rapid-scan NMR looked in the early 1970s, it was soon eclipsed by Fourier-Transform NMR due to the wide range of pulse sequences that became available.[13]

The first observation of transient effects, so called "wiggles", in EPR was made by Beeler et al.[14] in 1956. In 1960 an extensive article on various transient effects and spectral distortions was written by Weger[15] and this article still remains the only extensive review of passage effects in magnetic resonance. Until 2010, when Hyde[16] reported his

results in frequency-swept rapid-scan at 94 GHz, all of the rapid-scan research was done in a field-swept mode, which bears severe limitations (such as low sweep rate, heating of the sample and eddy currents). However, since nowadays the microwave technology is capable of sustaining it, frequency-swept rapid-scan EPR research is highly desirable because it promises high degree of applicability to improve well-known and widely used techniques, such as the Dynamic Nuclear Polarization. Moreover, it can be used to extract relaxation times of thin films and oriented crystals at high frequencies, both of which is today either expensive and difficult or downright impossible. This technique also promises an improvement in the S/N ratio[17–19] and detection limit of quantitative EPR[20].

Dynamic Nuclear Polarization (DNP) is a phenomenon that can enhance greatly the NMR sensitivity[21,22] (several hundred times at least). There are several mechanisms of DNP, though all of them result from the transferring of electron spin polarization (from special polarizing agents, typically organic radicals) to nucleus. This process is strongly dependent on the electron spin relaxation of the polarizing agent. However, due to the instrument limitations, the spin dynamics of polarizing agents is studied very poorly at frequencies above 100 GHz, especially at frequencies of 263, 329 and 394 GHz, which correspond to NMR proton frequencies of 400, 500 and 600 MHz, respectively.

By this method the NMR sensitivity can be enhanced by factors of theoretically up to 658 or 2617 for ^{1}H NMR of ^{13}C NMR, respectively. The NMR enhancement that is achieved in practice is strongly determined by which polarizing agent is used. Therefore there is a great interest in optimizing these agents, and, concurrently their *in situ* characterization. Because NMR spectrometers employ fixed field magnets, conventional field-swept EPR measurement cannot be carried out in NMR magnets[23]. In contrast, frequency-swept EPR experiments could be carried out in NMR magnets and, furthermore, development of the rapid-scan method would allow for *in situ* determination of DNP relevant characteristics of the polarizing agents; some of these characteristics, such as relaxation times, are strongly dependent on molecular environment and thus could significantly differ when measured isolated and when mixed with the NMR sample.

For this thesis we chose to demonstrate the rapid-scan technique on organic radicals. The organic radicals which we used possess several qualities which we aimed to exploit: they are by far the simplest systems to research by EPR since they possess only one unpaired electron and generally narrow lines. They are also well researched, stable and produce relatively strong signal. We chose two specific radicals – Lithium Phthalocyanine and BDPA (α,γ-Bisdyphenylene-β-phenylallyl) complex with benzene. In general, organic radicals are used for spin labels, as DNP agents[24,25] etc.

In this thesis the frequency-swept rapid-scan theory and experiment are explained on results awaiting publication (O. Laguta, M. Tuček, J. van Slageren and P. Neugebauer. Multi-frequency rapid-scan EPR, manuscript in preparation). It is indeed revolutionary because we demonstrate the ability to surpass previous research in terms of used frequencies with the aim for experiments up to the Terahertz range (which enables us to conduct experiments on DNP relevant frequencies), as well as the ability to process the data.

In the first chapter the general theory of EPR is explained with special accent on relaxation since it is of prime importance to the rapid-scan research. General principles of the conventional EPR experiments are also mentioned. In the second chapter the rapid-

scan history and theory are thoroughly dealt with. In the third chapter the experiment is described, including the home-built Multi-frequency High-Field EPR spectrometer and the experimental procedure. In the last chapter the results are presented and discussed.

2 General theory of EPR

In this chapter the general theory of EPR is dealt with. These basics are necessary to understand the theoretical background of the experiments described later. In sec.2.1 the paramagnetic resonance and Zeeman effect are explained. Then in sec.2.2 the quantum mechanical treatment of the spin system is briefly explained. In sec.2.3 the relaxation mechanisms of the spin system is thoroughly explained. This chapter then ends with sec.2.4, where the main experimental regimes of EPR are briefly described with the aim to connect the rapid-scan experiments with the conventional EPR.

2.1 Resonance condition

2.1.1 Spin state

An electron in an atomic orbit carries an orbital angular momentum due to its motion about the nucleus. Associated with this angular momentum is an orbital magnetic dipole moment $\boldsymbol{\mu}_{\mathrm{L}}$ proportional to the orbital angular momentum, which is denoted by $\boldsymbol{L}$, in a manner

$$\boldsymbol{\mu}_{\mathrm{L}} = -\mu_{\mathrm{B}}\boldsymbol{L}, \tag{2.1}$$

where μ_{B} is the Bohr magneton, given by

$$\mu_{\mathrm{B}} = \frac{e\hbar}{2m_{\mathrm{e}}} = 9.274015 \times 10^{-24}\,\mathrm{J}\cdot\mathrm{T}^{-1}, \tag{2.2}$$

where m_{e} is the electron mass. The electron also possesses an intrinsic angular momentum called the electron spin. The resulting spin magnetic dipole is given by

$$\boldsymbol{\mu}_{\mathrm{S}} = -g_{\mathrm{e}}\mu_{\mathrm{B}}\boldsymbol{S}, \tag{2.3}$$

where g_{e} is the electronic g-factor and $\boldsymbol{S}$ is the electron spin angular momentum. The total magnetic dipole momentum is then

$$\boldsymbol{\mu} = -\mu_{\mathrm{B}}(\boldsymbol{L} + g_{\mathrm{e}}\boldsymbol{S}). \tag{2.4}$$

In atomic systems angular momenta are quantized. The spin angular momentum obeys

$$\boldsymbol{S}^2 = S(S+1)\hbar^2, \tag{2.5}$$

where S is the spin quantum number. Then the magnetic spin quantum number m_{S} in general follows $m_{\mathrm{S}} = -S, (-S+1), ..., +S$. An electron has $S = 1/2$, therefore it can inhabit states given by magnetic quantum numbers of values $m_{\mathrm{S}} = \pm 1/2$.

The energy of a magnetic dipole in a static magnetic field $\boldsymbol{B}_0$ oriented along the z-axis, where $\boldsymbol{B}_0 = (0, 0, B_0)$, is

$$E = -\boldsymbol{\mu}\cdot\boldsymbol{B}_0 \tag{2.6}$$

$$E = -\mu_{\mathrm{z}}B_0 \tag{2.7}$$

and since the dimensionless quantization of spin along the z-axis is $S_z = m_s$, from equations (2.4) and (2.7) we obtain the energy of a specific electronic spin state as

$$E_S = g_e \mu_B B_0 m_S. \tag{2.8}$$

If a nucleus has simultaneously even number of protons and even number of neutrons, it has no spin value. In other cases it has a spin and the same principles as for the electron spin apply. Generally, the nuclei can possess spin numbers I of integer or half-integer values, and consequently the magnetic spin quantum numbers are $m_I = -I, -I+1, ..., +I$. This will be useful later when we discuss hyperfine splitting.

2.1.2 The Zeeman effect

The Zeeman effect describes splitting of energy levels of electrons and nuclei induced by a static external magnetic field (see fig.2.1). The energy difference between two spin states is

$$\Delta E_S = g_e \mu_B B_0 \Delta m_S = g_e \mu_B B_0, \tag{2.9}$$

from which the fundamental equation of paramagnetic resonance, the resonance condition, is produced. This equation states that a photon can excite the spin of an electron into a higher energy state if its energy equals the energy gap between the two states:

$$h\nu_{EPR} = g_e \mu_B B_0. \tag{2.10}$$

Here ν_{EPR} is the frequency of the applied electromagnetic wave.

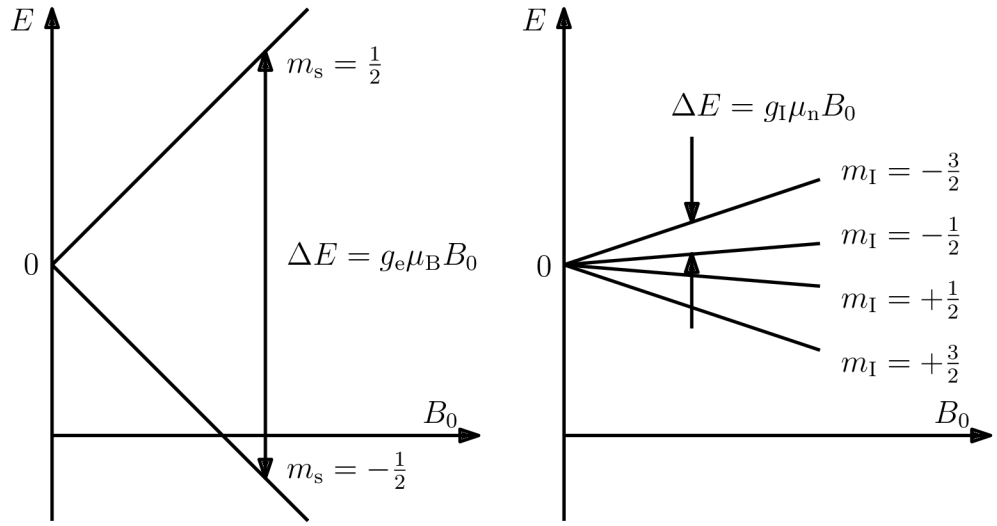

Figure 2.1: (left) Electron Zeeman levels for $S = 1/2$ as a function of the static magnetic field B_0. The magnetic dipole transition of the basic EPR experiment is indicated by an arrow at $B_0 = \Delta E/g_e\mu_B$. (right) Nuclear Zeeman levels for $I = 3/2$ as a function of the static magnetic field B_0. The energy difference for NMR transition $B_0 = \Delta E/g_n\mu_n$ is indicated.

Similarly, the resonance condition for nuclear spin transitions is

$$h\nu_{NMR} = g_n \mu_n B_0, \tag{2.11}$$

where g_n is the nuclear g-factor, which can be positive or negative, and μ_n is the nuclear magneton given by

$$\mu_\mathrm{n} = \frac{e\hbar}{2m_\mathrm{p}} = \frac{m_\mathrm{e}}{m_\mathrm{p}}\mu_\mathrm{B} \approx \frac{\mu_\mathrm{B}}{1836}, \tag{2.12}$$

where m_p is the proton mass. The energy needed for a nuclear spin state transition is therefore roughly 3 orders of magnitude lower than that needed for an electronic spin transition.

2.2 General spin Hamiltonian for EPR

The spin Hamiltonian is a quantum-mechanical way of describing the spin system under examination. It contains the operators of electron and nuclear spins, which may interact and contribute to the energy of the system. It also contains components of the magnetic field and may contain elements of external stress and electric fields.

In general, the spin Hamiltonian describing the system can be written as a sum of most important five components[26]:

$$\mathcal{H} = \mathcal{H}_\mathrm{EZI} + \mathcal{H}_\mathrm{FSI} + \mathcal{H}_\mathrm{HFI} + \mathcal{H}_\mathrm{NZI} + \mathcal{H}_\mathrm{QI}. \tag{2.13}$$

The electron Zeeman interaction is described as

$$\mathcal{H}_\mathrm{EZI} = \mu_\mathrm{B}\hat{S} \cdot \widetilde{g} \cdot \hat{B}, \tag{2.14}$$

where $\hat{S}$ is the electron spin operator, $\widetilde{g}$ is the g-tensor and $\hat{B}$ is the external magnetic field operator, describes the energy levels splitting caused by the external magnetic field. The fine structure interaction is described as

$$\mathcal{H}_\mathrm{FSI} = \hat{S} \cdot \widetilde{D} \cdot \hat{S}, \tag{2.15}$$

where $\widetilde{D}$ is the traceless fine structure (or zero-field interaction) tensor, describes the interaction of the spin system with the electric field created by ions of the environment (crystal or ligand field). This interaction is independent on the external magnetic field $\boldsymbol{B}_0$.
The hyperfine interaction is described as

$$\mathcal{H}_\mathrm{HFI} = \hat{I} \cdot \widetilde{A} \cdot \hat{S}, \tag{2.16}$$

where $\hat{I}$ is the nuclear spin operator and $\widetilde{A}$ is the hyperfine interaction tensor, describes the interaction of nuclear spin magnetic dipole with the electron spin magnetic dipole. The splitting of energy levels is illustrated in fig.2.2.
The nuclear Zeeman interaction is described as

$$\mathcal{H}_\mathrm{NZI} = \mu_\mathrm{n}\hat{I} \cdot \widetilde{g}_\mathrm{n} \cdot \hat{B} \tag{2.17}$$

describes the splitting of spin energy levels in nucleus, if it has any non-zero spin value, in external magnetic field B_0.
The nuclear quadrupole interaction is described as

$$\mathcal{H}_\mathrm{QI} = \hat{I} \cdot \widetilde{Q} \cdot \hat{I}, \tag{2.18}$$

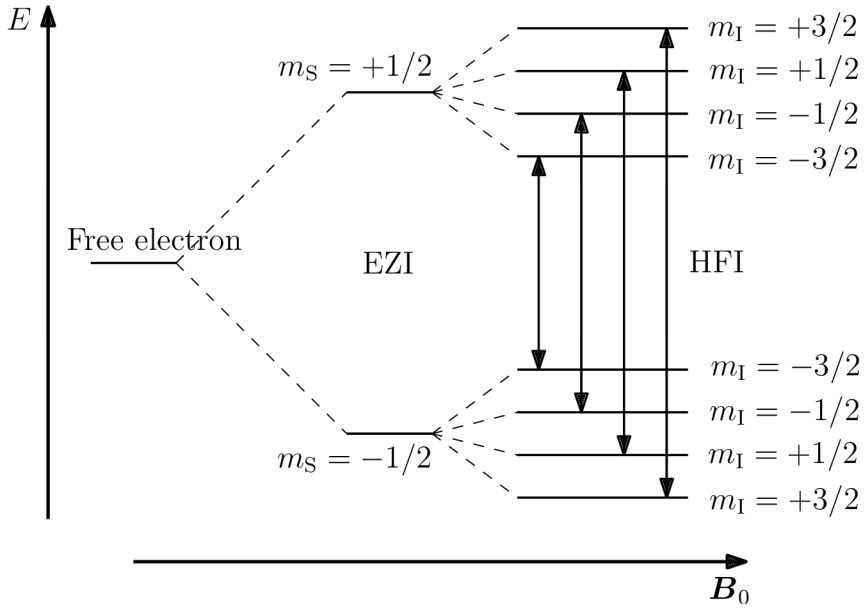

Figure 2.2: The splitting of electron energy levels in external magnetic field B_0 due to electron Zeeman effect and then further due to hyperfine interaction with a nucleus with $I = 3/2$. The arrows denote the allowed transitions ($\Delta m_S = \pm 1$, $\Delta m_I = 0$.)

where $\widetilde{Q}$ is the traceless nuclear quadrupole tensor, describes the interaction of the electric quadrupole moment of nuclei with spin $I > 1/2$ with the electric field gradient. This field gradient arises from uneven distributions of electric charges around the nucleus.

Usually the splitting arisen from $\mathcal{H}_{\mathrm{HFI}}$, $\mathcal{H}_{\mathrm{NZI}}$ and $\mathcal{H}_{\mathrm{QI}}$ is considerably smaller than that of electron Zeeman interaction and often can be neglected. The magnitude of said interactions can be sorted as follows: $\mathcal{H}_{\mathrm{EZI}} \geq \mathcal{H}_{\mathrm{FSI}} \gg \mathcal{H}_{\mathrm{HFI}} > \mathcal{H}_{\mathrm{NZI}} > \mathcal{H}_{\mathrm{QI}}$.

The gain in introducing the concept of spin Hamiltonian is the ability to analyze the EPR spectra without a detailed knowledge of the true wave function of the examined system[27], which is abundantly exploited by simulation softwares (e.g. EasySpin[28]). Parts of information about the true wave function are hidden in the interaction tensors $\widetilde{g}$, $\widetilde{A}$ and $\widetilde{D}$[27]. This is important for theoretical interpretation of the interaction parameters or constants.

2.3 Relaxation

2.3.1 Statistical approach

In this section the properties of a two-level spin system are examined. The system is defined as an ensemble of spins with $S = 1/2$ (electrons or protons), which are isolated (direct spin-spin interactions are negligible). A uniform external magnetic field is assumed, so the two energy levels are separated by $\Delta E = E_{\mathrm{u}} - E_{\mathrm{l}}$, where the "u" and "l" subscripts denote the upper and lower energy level, respectively. Only the corresponding Zeeman term in the spin Hamiltonian is considered, so that $\Delta E = g_{\mathrm{e}} \mu_{\mathrm{B}} B_0$.

A thermodynamic parameter called the spin temperature T_S, is defined by

$$\frac{N_u}{N_l} = \exp\left(-\frac{\Delta E}{k_B T_S}\right) \tag{2.19}$$

where N_u and N_l denote the population of the upper and lower levels and k_B is the Boltzmann constant. The ΔE stands for energy separation of the two states.

If the spin system is subjected to a pulse of electromagnetic radiation of energy matching the energy difference ΔE between the spin energy levels, the resulting EPR energy absorption by the spins cause a change in the populations – the ratio N_u/N_l is altered. The spin has gained energy, therefore it can be considered "hot" compared to its surroundings.

The spin system then undergoes various interactions with its surroundings by which it cools down (loses energy) and its spin temperature T_S is eventually restored to the temperature T of the surroundings. The loss of energy, considering the system receives an extra energy δE_0 by irradiating at time $t = t_0$, is depicted in fig.2.3 and is also described by exponential decay

$$\delta E = \delta E_0 \exp\left(-\frac{t - t_0}{T_1}\right) \tag{2.20}$$

where T_1 is the characteristic time for the energy flow from the spin system into the surroundings. This relaxation time T_1 reflects the degree of connection of the spin system to its surroundings.

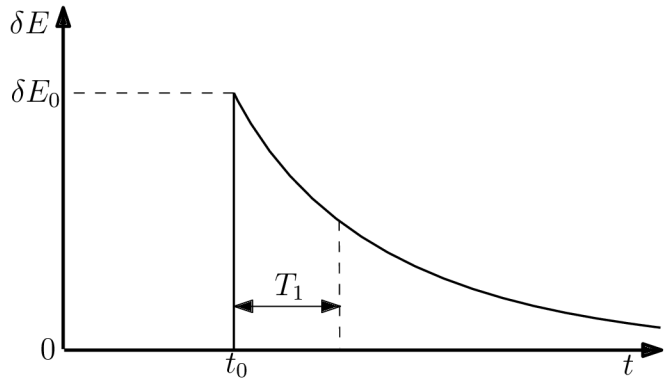

Figure 2.3: Temporal decay of the extra energy δE_0 in the system. Here t_0 denotes the time of energy influx into the system and T_1 stands for a measure of connection of the spin system to its surroundings.

Spin dynamics

Let us consider the population difference

$$\Delta N = N_u - N_l \tag{2.21}$$

as a single variable $\Delta N(B, T_S)$. Then

$$N_u = \tfrac{1}{2}(N - \Delta N) \tag{2.22}$$

$$N_l = \tfrac{1}{2}(N + \Delta N) \tag{2.23}$$

where $N = N_u + N_l$ is to total number of examined spins.

The probabilities per spin in unit time for upward and downward transition are denoted as $Z_\uparrow$ and $Z_\downarrow$. Then the differential rate law for this kinetic system is

$$\frac{\mathrm{d}\Delta N}{\mathrm{dt}} = -2N_\mathrm{l}Z_\uparrow + 2N_\mathrm{u}Z_\downarrow. \tag{2.24}$$

Here the first term is the rate of upward transitions and the second term the rate of downward transitions. This equation can be rewritten as

$$\begin{aligned}\frac{\mathrm{d}\Delta N}{\mathrm{dt}} &= N(Z_\downarrow - Z_\uparrow) - \Delta N(Z_\downarrow + Z_\uparrow) \\ &= \left(N\frac{Z_\downarrow - Z_\uparrow}{Z_\downarrow + Z_\uparrow} - \Delta N\right)(Z_\downarrow + Z_\uparrow).\end{aligned} \tag{2.25}$$

The system approaches a steady state, denoted by the "ss" superscript. By setting $\mathrm{d}\Delta N/\mathrm{dt} = 0$ we obtain

$$\Delta N^{ss} = N_\mathrm{l}^\mathrm{ss} - N_\mathrm{u}^\mathrm{ss} = N\frac{Z_\downarrow - Z_\uparrow}{Z_\downarrow + Z_\uparrow}. \tag{2.26}$$

Equation (2.25) then becomes

$$\frac{\mathrm{d}\Delta N}{\mathrm{dt}} = (\Delta N^\mathrm{ss} - \Delta N)(Z_\downarrow + Z_\uparrow). \tag{2.27}$$

The quantity $(Z_\downarrow + Z_\uparrow)^{-1}$ has a dimension of time and is by definition[1] the relaxation time T_1. Therefore

$$\frac{\mathrm{d}\Delta N}{\mathrm{dt}} = \frac{(\Delta N^\mathrm{ss} - \Delta N)}{T_1}. \tag{2.28}$$

This is a first order kinetic equation with the solution

$$\Delta N(t) = (\Delta N)_0 + [\Delta N^\mathrm{ss} - (\Delta N)_0]\left\{1 - \exp\left[-\frac{t - t_0}{T_1}\right]\right\}, \tag{2.29}$$

meaning that $\Delta N(t)$ evolves exponentially from $(\Delta N)_0$ toward ΔN^{ss} with a rate constant T_1, which is now seen to be the time required for ΔN to change by $[\Delta N^{ss} - (\Delta N)_0]\,[1 - e^{-1}]$[1]. From the definition of T_1 as the inverse of the sum of the transition probabilities per unit time, it can be safely said that T_1 is related to the mean lifetime of a given spin orientation state.This lifetime limitation has an effect on the linewidth broadening due to the Heisenberg uncertainty principle.

Relaxation mechanisms for T_1

Several mechanisms contribute to the upward and downward transition probabilities $Z_\uparrow$ and $Z_\downarrow$ specified as

$$Z_\uparrow = B_\mathrm{lu}\rho_\nu + W_\uparrow \tag{2.30}$$

$$Z_\downarrow = A_\mathrm{ul} + B_\mathrm{ul}\rho_\nu + W_\downarrow \tag{2.31}$$

where ρ_ν is the time-averaged radiation density to which the spin system is exposed, $W_\uparrow$ and $W_\downarrow$ are the upward and downward transition probabilities for transitions caused by surroundings, A_{ul} is the Einstein coefficient for spontaneous photon emission, B_{lu} and B_{ul} are Einstein coefficients for spontaneous absorption and emission and here $B_{\mathrm{lu}} = B_{\mathrm{ul}}$. We then receive[1]

$$\Delta N^{\mathrm{ss}} = N \frac{A_{\mathrm{ul}} + W_\downarrow - W_\uparrow}{A_{\mathrm{ul}} + 2B_{\mathrm{ul}}\rho_\nu + W_\downarrow + W_\uparrow} \tag{2.32}$$

$$T_1 = (A_{\mathrm{ul}} + 2B_{\mathrm{ul}}\rho_\nu + W_\downarrow + W_\uparrow)^{-1}. \tag{2.33}$$

If the radiation density term ρ_ν dominates in $Z_\uparrow$ and $Z_\downarrow$ these become equal and $\Delta N \Longrightarrow \Delta N^{\mathrm{ss}} \Longrightarrow 0$, hence no net absorption of radiation by the spins is observed, the EPR signal disappears. This is called power saturation and the importance of having an adequate relaxation mechanism and of applying only moderate microwave field is obvious.

There are several mechanisms of spin-lattice relaxation, which all involve interactions of the spin system with phonons. The most important involve:

1. *Direct processes.* This mechanism dominates only at very low temperatures and involves direct phonon-assisted non-radiative transitions.

2. *Raman processes.* This becomes increasingly more important as the temperature increases; involves virtual excitation followed by relaxation to phonon states of much higher energy than the spin level.

3. *Orbach processes.* If a low lying spin level exists at an energy Δ above the ground state, a Raman process involving that state can dominate the spin-lattice relaxation[29,30].

4. *Other processes.* Several other mechanisms have been proposed. In gases, collisions are an important mechanism of relaxation[31].

2.3.2 Bloch model

The famous Bloch equations[32] offer another view of relaxation. They describe the time dependence of the total spin magnetization vector $\boldsymbol{M}$ in the presence of static external magnetic field and oscillating microwave field. The equations are especially useful, because they

- Offer a visual and intuitive model of vectors and torques in the description of the resonance phenomenon. A rotating frame of reference is introduced.

- Significantly simplify the complex spin interactions with the surroundings by gathering the aspects into just two empirical parameters – the relaxation times T_1 and T_2.

- Serve well by introducing the important concepts of absorption and dispersion.

- Are useful in describing the whole ensemble of spins and gracefully lead into the topic of interconversion between two ensembles.[1]

They do of course have limitations. They cannot be employed to visualize the quantum-mechanical behaviour of individual spins – thus the consideration of spin-spin coupling, hyperfine interactions, anisotropies of the medium etc. are excluded.

Motion of magnetization

The time dependence of the general angular momentum operator $\boldsymbol{J}$ in the Heisenberg picture follows from quantum mechanics as

$$\frac{\mathrm{d}\boldsymbol{J}}{\mathrm{d}t} = \frac{i}{\hbar}\left[\mathcal{H}, \boldsymbol{J}\right] = \frac{i}{\hbar}\left(\mathcal{H}\boldsymbol{J} - \boldsymbol{J}\mathcal{H}\right), \tag{2.34}$$

where $\mathcal{H}$ is the Hamiltonian operator for the system. Again, we consider only the Zeeman term constituting the spin Hamiltonian, so the description of the electrons' coupling to the external magnetic field $\boldsymbol{B}_0 = (0, 0, B_0)$ is

$$\mathcal{H}_\mathrm{S} = g_\mathrm{e}\mu_\mathrm{B}B_0S_\mathrm{z}. \tag{2.35}$$

The time dependence of $\boldsymbol{S}$ for B_0 parallel to the z-axis is then

$$\frac{\mathrm{d}\boldsymbol{S}}{\mathrm{d}t} = \frac{i}{\hbar}\left[\mathcal{H}, \boldsymbol{S}\right] = \frac{i}{\hbar}g_\mathrm{e}\mu_\mathrm{B}B_0\begin{pmatrix}[S_\mathrm{z}, S_\mathrm{x}]\\ [S_\mathrm{z}, S_\mathrm{y}]\\ [S_\mathrm{z}, S_\mathrm{z}]\end{pmatrix} = \frac{g_\mathrm{e}\mu_\mathrm{B}B_0}{\hbar}\begin{pmatrix}-S_\mathrm{y}\\ +S_\mathrm{x}\\ 0\end{pmatrix}. \tag{2.36}$$

This can then be rewritten into a vector form as

$$\frac{\mathrm{d}\boldsymbol{S}}{\mathrm{d}t} = -\frac{g_\mathrm{e}\mu_\mathrm{B}}{\hbar}\left(\boldsymbol{B}_0 \times \boldsymbol{S}\right). \tag{2.37}$$

However, in the EPR experiments, a single electron is never measured. It is necessary to describe a whole ensemble of spins. Therefore we must deal with the quantum mechanical expectation values and their motion rather than with the motion of a single particle operator as described above.
The expectation value of $\boldsymbol{\mu}_\mathrm{S}$ is the macroscopic magnetization $\boldsymbol{M}$ given by

$$\boldsymbol{M} = \langle\boldsymbol{\mu}_\mathrm{S}\rangle = g_\mathrm{e}\mu_\mathrm{B}\langle\boldsymbol{S}\rangle \tag{2.38}$$

and

$$\hbar\frac{\mathrm{d}\langle\boldsymbol{S}\rangle}{\mathrm{d}t} = g_\mathrm{e}\mu_\mathrm{B}\left(\langle\boldsymbol{S}\rangle \times \boldsymbol{B}_0\right). \tag{2.39}$$

Thus we obtain the equation of motion for the magnetization

$$\frac{\mathrm{d}\boldsymbol{M}}{\mathrm{d}t} = \gamma\boldsymbol{M} \times \boldsymbol{B}_0, \tag{2.40}$$

where γ is the gyromagnetic ratio of an electron defined as $\gamma = g_\mathrm{e}\mu_\mathrm{B}/\hbar$.

The magnetization $\boldsymbol{M}$ is invariant if it is aligned along the z-axis. Otherwise, there is always a torque $\boldsymbol{\tau} = \boldsymbol{M} \times \boldsymbol{B}_0$, perpendicular to $\boldsymbol{M}$, which causes it to precess on a cone about $\boldsymbol{B}_0$. The frequency of such precession, which is called the Larmor frequency, in angular frequency units is

$$\omega_\mathrm{S} = \gamma B_0, \tag{2.41}$$

and is also identical to the frequency which follows from the resonance condition (2.10), by replacing $h\nu$ with $\hbar\omega$.

Rotating frame

Let us now view the motion of magnetization $\boldsymbol{M}$ in a system of coordinates rotating with angular velocity $\boldsymbol{\omega}$ relative to a laboratory stationary system. Then the rate of variation of $\boldsymbol{M}$ in the laboratory frame is related to its rate of variation in the rotating system through the equation[33]

$$\left(\frac{\mathrm{d}\boldsymbol{M}}{\mathrm{dt}}\right)_{\mathrm{lab}} = \left(\frac{\mathrm{d}\boldsymbol{M}}{\mathrm{dt}}\right)_{\mathrm{rot}} + \boldsymbol{\omega} \times \boldsymbol{M} \tag{2.42}$$

which when combined with eq.(2.40) yields the equation of motion in the rotating system

$$\left(\frac{\mathrm{d}\boldsymbol{M}}{\mathrm{dt}}\right)_{\mathrm{rot}} = \left(\frac{\mathrm{d}\boldsymbol{M}}{\mathrm{dt}}\right)_{\mathrm{lab}} - \boldsymbol{\omega} \times \boldsymbol{M} = \gamma \boldsymbol{M} \times (\boldsymbol{B}_0 + \boldsymbol{\omega}/\gamma)\,. \tag{2.43}$$

Thus the motion relative to the rotating system will again be a precession, but with angular velocity

$$\boldsymbol{\Omega}_{\mathrm{S}} = -\gamma \boldsymbol{B}' = -\gamma\,(\boldsymbol{B}_0 + \boldsymbol{\omega}/\gamma) = \boldsymbol{\omega}_{\mathrm{S}} - \boldsymbol{\omega}. \tag{2.44}$$

The apparent precession velocity is equal to the difference between $\boldsymbol{\omega}_{\mathrm{S}}$, the angular velocity observed in the stationary system, and $\boldsymbol{\omega}$, the velocity of the rotating coordinate system relative to the fixed one. This is equivalent to saying that in the rotating system there is an effective magnetic field parallel to the z-axis

$$\boldsymbol{B}' = \boldsymbol{B}_0 + \boldsymbol{\omega}/\gamma = \boldsymbol{B}_0 - \boldsymbol{B}^*, \tag{2.45}$$

where $\boldsymbol{B}^* = -\boldsymbol{\omega}/\gamma$. If $\boldsymbol{\omega} = \boldsymbol{\omega}_{\mathrm{S}}$, the precession vanishes and $\boldsymbol{M}$ is at rest in the rotating frame system, corresponding to the effective field $\boldsymbol{B}'$ being zero.

This result enables us to derive simply the motion of magnetization under the combined action of steady field $\boldsymbol{B}_0$, parallel to the z-axis, and a field $\boldsymbol{B}_1$ rotating with angular frequency $\boldsymbol{\omega}$ about the z-axis. In the rotating system, the field $\boldsymbol{B}_1$ is a constant vector normal to the z-axis, as in fig.2.4. At the same time the constant field $\boldsymbol{B}_0$ is replaced by the effective field $\boldsymbol{B}'$, which may be conveniently written as $\boldsymbol{B}' = \boldsymbol{B}_0 - \boldsymbol{B}^*$.
The couple acting on the magnetization is now

$$\frac{\mathrm{d}\boldsymbol{M}}{\mathrm{dt}} = \gamma \boldsymbol{M} \times (\boldsymbol{B}' + \boldsymbol{B}_1) = \gamma \boldsymbol{M} \times \boldsymbol{B}_{\mathrm{eff}} \tag{2.46}$$

where $\boldsymbol{B}_{\mathrm{eff}} = \boldsymbol{B}' + \boldsymbol{B}_1$. Hence referred to the rotating system, $\boldsymbol{M}$ will undergo a precession about the $\boldsymbol{B}_{\mathrm{eff}}$ with angular velocity $-\gamma \boldsymbol{B}_{\mathrm{eff}}$ and assume that the rotating field $\boldsymbol{B}_1$ is switched on suddenly, when the magnetization is aligned along $\boldsymbol{B}_0$. The motion of the magnetic moment is then a precession about $\boldsymbol{B}_1$ with angular velocity $-\gamma \boldsymbol{B}_1$ and every half-cycle of this motion the changes from being parallel to $\boldsymbol{B}_0$ to being anti-parallel and back again. In the rotating system this rotation takes place in the plane normal to $\boldsymbol{B}_1$. In general, $B_1 \ll B_0$, so that the precession about $\boldsymbol{B}_1$ occurs at a much lower velocity than that at which $\boldsymbol{B}_1$ rotates in the laboratory system. Thus, in this system, the motion of $\boldsymbol{M}$ consists of a rapid rotation about $\boldsymbol{B}_0$ at an angle α to $\boldsymbol{B}_0$ which varies slowly from 0 to π and back again.

When the frequency of rotation of $\boldsymbol{B}_1$ is not equal to the natural precession frequency $\boldsymbol{\omega}_{\mathrm{S}}$, the magnetization $\boldsymbol{M}$ precesses (in the rotating frame) about the field $\boldsymbol{B}_{\mathrm{eff}}$. This field makes and angle θ with $\boldsymbol{B}_0$, where

$$\tan\theta = \frac{B_1}{B'} = \frac{B_1}{B_0 - B^*} = \frac{B_1}{B_0 + \omega/\gamma} \tag{2.47}$$

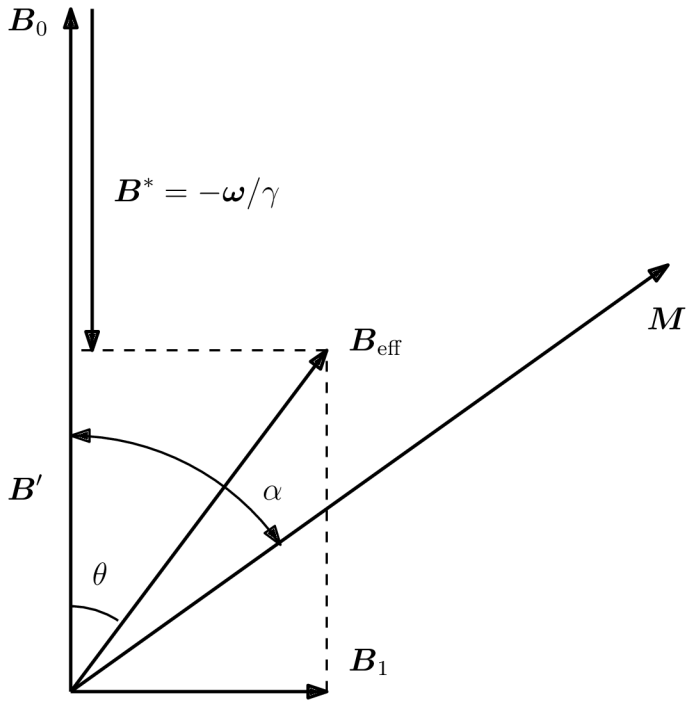

Figure 2.4: Effective fields in the rotating coordinate system. Taken from [33].

and from simple geometrical consideration the value of the angle α at time t (assuming $\alpha = 0$ at $t = 0$) is found to be

$$\begin{aligned} \cos\alpha &= \cos^2\theta + \sin^2\theta\cos(\gamma B_{\text{eff}} t) \\ &= 1 - 2\sin^2\theta\sin^2(\tfrac{1}{2}\gamma B_{\text{eff}} t) \end{aligned} \tag{2.48}$$

where

$$\gamma B_{\text{eff}} = \left(\Omega_{\text{S}}^2 + \gamma^2 B_1^2\right)^{\frac{1}{2}} \tag{2.49}$$

The maximum value attained by α is clearly 2θ, and if $B_1 \ll B_0$ (which is normally the case) this value is large only when we are correspondingly close to fulfilling the condition $\Omega_{\text{S}} = 0$, which is a resonance effect and the possibility of being able to change the orientation of the magnetization $\boldsymbol{M}$ with respect to the steady field $\boldsymbol{B_0}$ by the application of a relatively small rotating field $\boldsymbol{B}_1$ constitutes the phenomenon of magnetic resonance. When $\Omega_{\text{S}} = 0$, the magnetization $\boldsymbol{M}$, assumed to be initially parallel to $\boldsymbol{B}_0$, can be completely reversed by application of the rotating field $\boldsymbol{B}_1$; in the ideal case this will occur no matter how small the value of $\boldsymbol{B}_1$ is, though the rate of reversal is of course proportional to $\boldsymbol{B}_1$. [33]

It is convenient for further use to rewrite the eq.(2.40), the motion of magnetization $\boldsymbol{M}$ in the rotating frame, into axes-separated form [34]

$$\begin{aligned} \frac{\mathrm{d}M_x}{\mathrm{dt}} &= -(\omega_{\text{S}} - \omega)M_y = -\Omega_{\text{S}} M_y \\ \frac{\mathrm{d}M_y}{\mathrm{dt}} &= (\omega_{\text{S}} - \omega)M_x - \frac{g_{\text{e}}\mu_{\text{B}} B_1}{\hbar} M_z = \Omega_{\text{S}} M_x - \omega_1 M_z \\ \frac{\mathrm{d}M_z}{\mathrm{dt}} &= \frac{g_e \mu_B B_1}{\hbar} M_y = \omega_1 M_y. \end{aligned} \tag{2.50}$$

In the next section these equations will be used to derive the fundamental set of equations fully describing the motion of magnetization of an ensemble of spins – the Bloch equations.

Relaxation times

So far it was assumed that once the spin system has been excited, the precession of the magnetization vector goes on forever. Let us now assume instead that the spin system tends to achieve thermal equilibrium at some point in time. In a static field the trend towards the system's equilibrium value $M_z = M_0$ can be described with good accuracy by the equation

$$\frac{\mathrm{d}M_z}{\mathrm{dt}} = \frac{-\left(M_z - M_0\right)}{T_1}, \tag{2.51}$$

where T_1 is the longitudinal (or spin-lattice) relaxation time. If by any means, such as microwave pulse, the magnetization is given a component at right angles to the applied field B_0, the various local fields, owing to the fact that the spins are actually not free but interact with each other and with their surroundings, cause the transverse magnetization to decay at a rate, which can be represented by equations:

$$\frac{\mathrm{d}M_x}{\mathrm{dt}} = -\frac{M_x}{T_2} \tag{2.52}$$

$$\frac{\mathrm{d}M_y}{\mathrm{dt}} = -\frac{M_y}{T_2}. \tag{2.53}$$

The T_2 stands for the transverse (or spin-spin) relaxation time. Both of T_1 and T_2 are unique to each material and dependent on temperature, magnetic field and surroundings. These relaxation times describe relaxation of the whole ensemble of spins.

In the presence of an applied field and much smaller microwave field, the motion due to relaxation can be superposed on the motion of the free spins, leading to the fundamental system of equations for paramagnetic resonance, the Bloch equations:

$$\begin{aligned}
\frac{\mathrm{d}M_x}{\mathrm{dt}} &= -\Omega_{\mathrm{S}} M_y - \frac{M_x}{T_2} \\
\frac{\mathrm{d}M_y}{\mathrm{dt}} &= \Omega_{\mathrm{S}} M_x - \omega_1 M_z - \frac{M_y}{T_2} \\
\frac{\mathrm{d}M_z}{\mathrm{dt}} &= \omega_1 M_y - \frac{\left(M_z - M_0\right)}{T_1}.
\end{aligned} \tag{2.54}$$

This system of equations is of high importance since it completely describes the dynamics of the magnetic moment.

Steady-state solution of Bloch equations

The general solution, for fixed values of the parameters, is a sum of decreasing exponential terms and of a steady-state solution obtained by setting

$$\frac{\mathrm{d}M_x}{\mathrm{dt}} = \frac{\mathrm{d}M_y}{\mathrm{dt}} = \frac{\mathrm{d}M_z}{\mathrm{dt}} = 0. \tag{2.55}$$

If a sufficiently long time has elapsed for the transient exponentials to have decayed, the steady-state solution can be written as

$$M_x = \frac{\Omega_S \gamma B_1 T_2^2}{1 + (T_2\Omega_S)^2 + \gamma^2 B_1^2 T_1 T_2} M_0 \tag{2.56}$$

$$M_y = \frac{\gamma B_1 T_2}{1 + (T_2\Omega_S)^2 + \gamma^2 B_1^2 T_1 T_2} M_0 \tag{2.57}$$

$$M_z = \frac{1 + (T_2\Omega_S)^2}{1 + (T_2\Omega_S)^2 + \gamma^2 B_1^2 T_1 T_2} M_0 \tag{2.58}$$

The transformation back to the laboratory frame *x', y', z'* yields

$$\boldsymbol{M'} = \begin{pmatrix} M_{x'} \\ M_{y'} \\ M_{z'} \end{pmatrix} = \begin{pmatrix} M_x \cos(\omega t) + M_y \sin(\omega t) \\ -M_x \sin(\omega t) + M_y \cos(\omega t) \\ M_z \end{pmatrix}. \tag{2.59}$$

The transverse magnetization component M_x rotates synchronously with B_1 about the z-axis, while the other transverse component M_y is shifted in its phase by 90° with respect to M_x. Therefore, considering the complex magnetic susceptibility

$$\chi = \chi' + \mathrm{i}\chi'', \tag{2.60}$$

M_x constitutes the dispersive part χ' and M_y constitutes the absorptive part χ'' as follows[27]:

$$\chi' = \frac{M_x}{2B_1}, \tag{2.61}$$

$$\chi'' = \frac{M_y}{2B_1}. \tag{2.62}$$

The phenomenon of dispersion always accompanies the resonant absorption of energy from the microwave field. Here the term *dispersion* denotes the real part of the magnetic susceptibility, whereas absorption is the measure of the imaginary part. Dispersion manifests itself in a shift in the resonant frequency of the cavity (or other resonator) in the spectrometer. Many conventional spectrometers have the source frequency-locked to the resonator's resonant frequency, so the dispersion is absent.

If the system is not power-saturated, that is if

$$\gamma^2 B_1^2 T_1 T_2 \ll 1, \tag{2.63}$$

we obtain a steady-state solution in the form of

$$\chi'' = \frac{\gamma T_2 M_0}{2(1 + \Omega_S^2 T_2^2)} \tag{2.64}$$

$$\chi' = \frac{\gamma \Omega_S T_2^2 M_0}{2(1 + \Omega_S^2 T_2^2)} \tag{2.65}$$

$$M_z = M_0. \tag{2.66}$$

The profile of χ' and χ'' is illustrated by fig.2.5. It is important to point out that $\chi'' = \chi'/(\Omega_S T_2)$ and that both depend on B as well as B_1 via the power-saturation term (see eq.(2.63)).

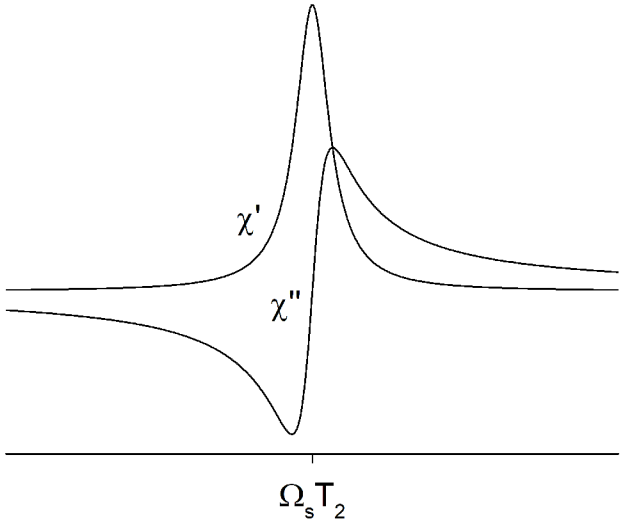

Figure 2.5: Line shape for the real and imaginary part of the complex magnetic susceptibility χ. The imaginary part χ'' has a Lorentzian line shape, which is the line shape measured for a homogeneous EPR.

2.3.3 Linewidths

Homogenenous broadening

Homogeneous line broadening for an ensemble of spins occur when all of these have the same spin-hamiltonian parameters and the external magnetic field has the same magnitude over the sample volume – in other words, if the transition probability as a function of magnetic field is the same for each dipole. The resulting line is usually lorentzian-shaped (see χ' in fig.2.5).

In general, an effective T_2 can be calculated by

$$T_2 = (\kappa\gamma\Delta\omega_{1/2})^{-1} \tag{2.67}$$

where $\Delta\omega_{1/2}$ is the half-width at half-maximum (in units of mT) and κ is a factor depending on the lineshape ($\kappa = 1$ for lorentzian, $\kappa = (\pi \ln 2)^{1/2}$ for gaussian).

It is necessary to return to consideration of the individual spins to further understand contributions to T_2. It has been said it is a measure of the interactions between spins. In this case, if $T_2 = \infty$, there is no interaction whatsoever (the spins are completely isolated), whereas $T_2 = 0$ implies very strong coupling with no local variations in spin temperature (this would be relevant to strongly coupled systems, such as ferromagnetic or antiferromagnetic). The spins can interact via magnetic dipolar coupling. Mutual spin flips of paired spins cause no change in energy of the spin system, but do affect the lifetime (characterized by T_1) of each spin[1]. The propagation of magnetization through the lattice via such flips is called *spin diffusion*; this causes equilibration to the same spin temperature throughout the ensemble of equivalent spins and the T_2 is a measure of this rate.

Inhomogeneous broadening

Generally the paramagnetic electrons in a sample are not subjected to the exact same B values – thus at any given time only a small fraction of spins is in the resonance as the external magnetic field passes through the "line". The observed line is then a superposition of a large number of individual components, called the *spin packets*, each slightly shifted from one another.

The following are some phenomena that can cause an inhomogeneous line broadening:

- An inhomogeneous external magnetic field.
- Unresolved hyperfine structure, occurring when the number of hyperfine components form nearby nuclei is so high that no structure is observed and only the envelope of a multitude of lines is detected.
- Anisotropic interactions in randomly oriented systems, such as polycrystals, powders, glasses etc. The anisotropic $\widetilde{g}$ and $\widetilde{A}$ can give rise to inhomogeneity. The observed result can be highly asymmetrical lines.
- Dipolar interactions with a paramagnetic center. This may impose a random local field at a given paramagnetic electron.[1]

2.4 General principles of experiments in EPR

Electron paramagnetic resonance is a potent and complicated method of investigating various materials and spin dynamics. There are many methods of conducting experiments, each one requiring highly sophisticated machines and deep knowledge to understand the observed phenomena. For the sake of simplicity we now describe two general EPR techniques and give short descriptive introduction into the principles of the experiments.

This section is by no means intended as a thorough description or division of the many various techniques and experiments used in the EPR field; it is rather intended as a soft introduction to the two specific aspects of EPR closely related to the rapid-scan technique.

2.4.1 Contiuous wave EPR

In continuous wave experiments (abbreviated as CW) the sample is put inside a magnet and the field is swept in such a slow manner that it can be considered steady. The microwave radiation is kept on a constant frequency (thus continuous wave) and after propagating through the optical path excites the spin system if the resonance condition (eq.(2.10)) is met.

To improve the signal-to-noise ratio, a low magnitude fast-oscillating external magnetic field is usually added to the main field. This is called "modulation" and causes the detection of a first derivative of the EPR lines (as shown in fig.2.6). Not only this significantly improves the S/N ratio, but also allows the observer to be able to evaluate the spectra more easily. The fig.2.6 illustrates what the first derivative spectrum can look like. The molecular structure of the measured molecule, called AMUPol and widely studied by Gast[35], is shown in fig.2.7.

This technique is used mainly as an analysis of a given material on a molecular level; understanding intra-molecular phenomena such as the g-tensor anisotropy, hyperfine splitting or exchange interaction and the inter-molecular phenomena, such as dipolar coupling. No phenomena related to relaxation can be directly observed.

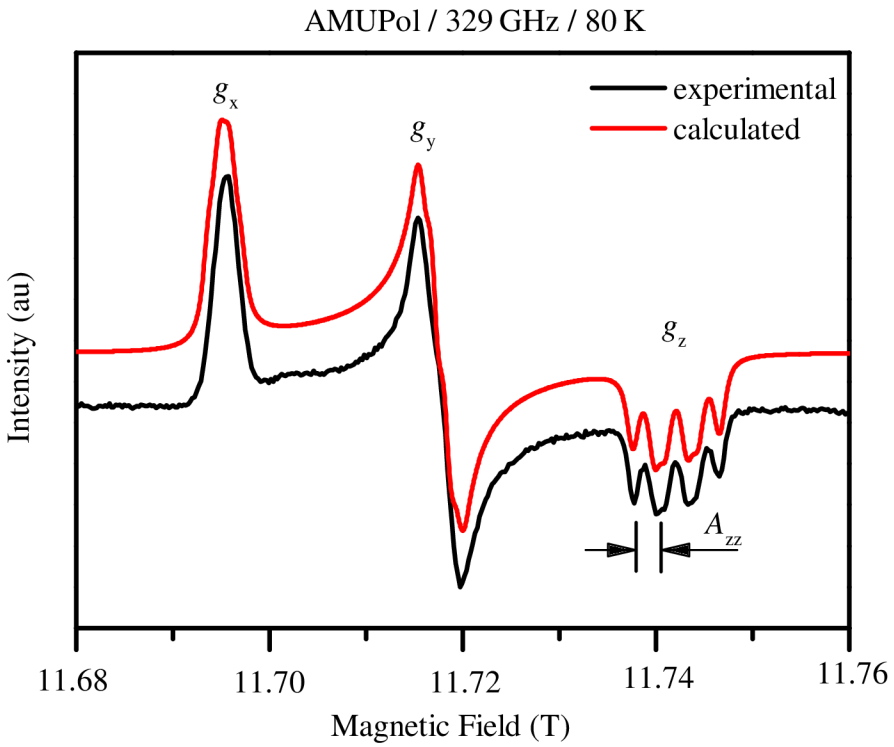

Figure 2.6: A first derivative spectrum of AMUPol measured at the home-built High Field EPR spectrometer[23] (black) and calculated by EasySpin[28] (red) at the University of Stuttgart. Anisotropy of $\widetilde{g}$ can be clearly observed as well as hyperfine splitting of a part of the spectrum. Measured at 329 GHz and at 80 K.

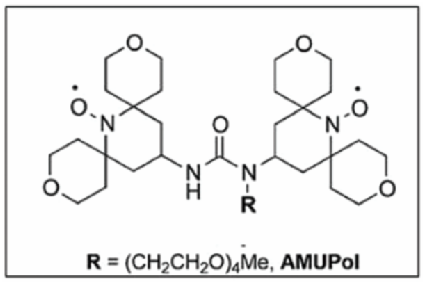

Figure 2.7: Molecular structure of a nitroxide biradical AMUPol, as studied by Gast[35] for the purposes of DNP.

2.4.2 Pulsed EPR

The general principles of pulsed techniques in EPR is keeping the external field constant and administering a high-power, short microwave pulse to the spin system. In case of a specific (so-called 90°) pulse the magnetization $\boldsymbol{M}$ is completely flipped from z-direction

to xy-plane, from where it then relaxes back to the z-direction while precessing about the z-axis with Larmor frequency. The resulting trajectory of the magnetization vector was first observed in nuclear magnetic resonance by inserting a detection coil into the xy-plane and reading out the voltage induced by the nuclear magnetization vector movement; this is depicted in fig.2.8.

The curve depicted in fig.2.8 is called the *free induction decay* (FID). It generally follows a formula

$$Y(t) \sim \exp\left(i\omega_{\mathrm{S}} t\right) \exp\left(-\frac{t - t_0}{T_2}\right) \tag{2.68}$$

where ω_{S} is the Larmor frequency, t denotes the time variable and T_2 is the spin-spin (transversal) relaxation time. The first term describes a circular precession about the z-axis. The exponential decay differs in the relaxation time used from eq.(2.29) because the decay of magnetization from the xy-plane is detected here and reading out the voltage induced by movement of $\boldsymbol{M}_{xy}$.

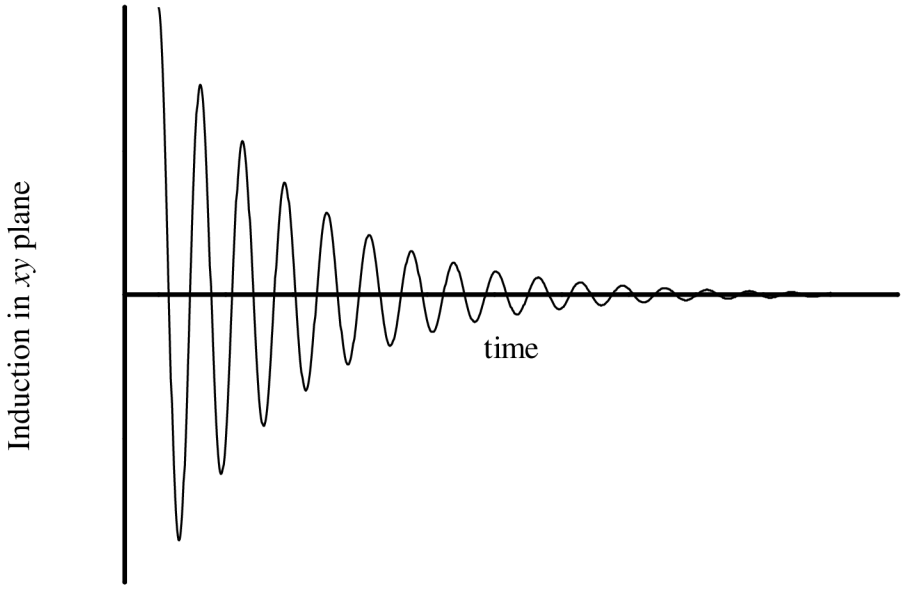

Figure 2.8: Observable relaxation of xy magnetization $\boldsymbol{M}_{xy}$ after a pulsed excitation. The exponential decay is proportional to T_2. At first observed in nuclear magnetic resonance by inserting a detection coil into the xy-plane.

The pulsed techniques are generally highly demanding on instrumentation. The introduction of a resonant cavity precisely tuned to the specific frequency used is necessary, which brings a size limitation to the sample; at 10 GHz, $\lambda = 3$ cm, while at 300 GHz, $\lambda = 1$ mm. Also a high-power microwave pulse source is required, which technologically limits the frequency range where the experiment can be conducted.

The FID's benefit we want to emphasize here is the ease of observing relaxation of the $\boldsymbol{M}_{xy}$ and consequent T_2 determination, because T_2 is essential for various quantum computing and spintronic applications.

3 Rapid-scan EPR

This chapter deals with the historical background and theoretical treatment of the rapid-scan regime. In the previous chapter the building blocks for understanding these concepts were hinted; here they will be elaborated on. The first part of this chapter, sec.3.1, deals with history, qualitative characterization and advantages of the rapid-scan regime. The second part, sec.3.2, describes the theoretical concepts behind the rapid-scan regime.

3.1 Introduction

Historically, most EPR experiments and instrumentation have been in one of two modes – continuous wave (CW) or pulsed (saturation recovery, spin echo and Fourier Transform are examples of techniques in the pulsed regime)[34]. In a CW experiment, the microwave power is constant and relatively low, and the magnetic field is slowly swept, with respect to relaxation times and modulation period, to achieve resonance. The signal is detected by phase-sensitive detection at the frequency that is used for magnetic field modulation. This additional external low-magnitude oscillating field ("modulation" field) is added to the slowly-swept one to achieve a drastic improvement in the S/N ratio. In pulse experiments the microwave power (high with respect to CW) is on only during short-term excitation and the signals are detected after the excitation.

The rapid-scan regime is an intermediate case. As in CW experiments, the microwave power is kept constant, but the microwave frequency (or magnetic field) is scanned through resonance in a time that is short compared to relaxation times. Phase sensitive detection and field modulation is not used; instead, the absorption and dispersion signals are recorded by direct detection.

Rapid-scan EPR builds on prior work in NMR (nuclear magnetic resonance). Bloembergen, Purcell and Pound[36] observed transient effects ("wiggles") in NMR spectra after the magnetic field passed through resonance. In 1974 it was shown that these transient effects can be deconvolved to obtain slow-scan NMR spectra[10,11]. Rapid-scan NMR achieved almost as high signal-to-noise ratio as pulsed Fourier-transform NMR with the advantage that rapid-scan NMR could measure a portion of a spectrum and hence avoiding a strong solvent peak. However, rapid-scan NMR was soon eclipsed by Fourier-transform NMR (Nobel Prize in Chemistry, 1991) due to the wide range of pulse sequences becoming available.

Transient effects were also observed in the early days of EPR. The first observation of "wiggles" in EPR was by Beeler et al.[14]. It was later shown that shapes of EPR spectra changed when the modulation period was comparable to T_2. Multiple passage effects were described by Weger[15] and although it was published almost 60 years ago, this article still remains the only extensive review of passage effects in magnetic resonance. In 2010, Hyde et al.[16] achieved rapid frequency-swept scans at 94 GHz on nitroxide radicals.

Current leader in the field of rapid-scan EPR is the group of Sandra S. Eaton and Gareth R. Eaton from the University of Denver. This group revisited the importance of rapid-scan for EPR and developed a field-swept rapid-scan technique (described by Stoner[37] in

2004), and until present continue to improve the method[17,20,38,39] and use it for research of radicals[18,40], mostly at X-band and ambient temperature.

Prior to the use of magnetic field modulation, EPR spectra were recorded as the voltage output of a diode detector as the magnetic field was swept. This is detection at the resonant frequency and is referred to as "direct detection", distinct from phase-sensitive detection at the field modulation frequency. The output is the absorption spectrum. This is also the method of detecting the rapid-scan measurements - the signal is recorded directly without phase-sensitive detection. The scans can be performed with magnetic field or microwave frequency sweeps such that the time on resonance is long or short relative to the electron spin relaxation times.

When the scan rate is slow relative to relaxation rates, and thus the time on resonance is long relative to the relaxation times, the absorption spectrum is detected. When the scan rate is fast relative to relaxation times, oscillations may be observed on the trailing edge of the signal (see fig.3.1). As the scan rate increases, the depth and number of oscillations increase and the signal broadens. Post-processing deconvolution can be then used to remove both the broadening and the oscillations and obtain the undistorted absorption spectra. Rapid-scan is analogous to pulsed EPR in the sense that the microwaves are resonant with the spins for only a brief period of time during the scan. Consequently, higher power can be used relative to a CW scan; the faster the scan, the shorter the time during which B_1 excites the spin packets, so the balance between excitation and relaxation favours relaxation and higher B_1 can be applied.

In this thesis, we describe a frequency-swept rapid-scan experiments at 200 GHz offset frequency with sweeps up to 26 GHz wide with maximum sweep rate of 61 500 THz/s (this corresponds to roughly 349 kT/s). This is revolutionary since it proves our ability to conduct the experiment at offset frequencies which are relevant for DNP (apart from other advantages of high-field and high-frequency experiments). The frequency-swept rapid-scan bears several advantages compared to the previously done field-swept rapid-scan:

1. Much higher sweep rates are possible (our maximum sweep rate of 61 500 THz/s corresponds to roughly 349 kT/s, compared to 11.8 T/s reported by Yu[17]). The microwave source technology has already surpassed the possibilities of magnetic sweeping coils in terms of stability and speed of produced scans.

2. It is possible to cover a relatively wide spectrum with one sweep.

3. The eddy currents in the sample holder and/or resonator are completely absent.

4. The temperature of the sample can be controlled far more easily since there is no sweeping coil producing excess heat; that allows for measurements at low temperatures.

5. The lack of resonating cavity lifts the limitations of sample size.

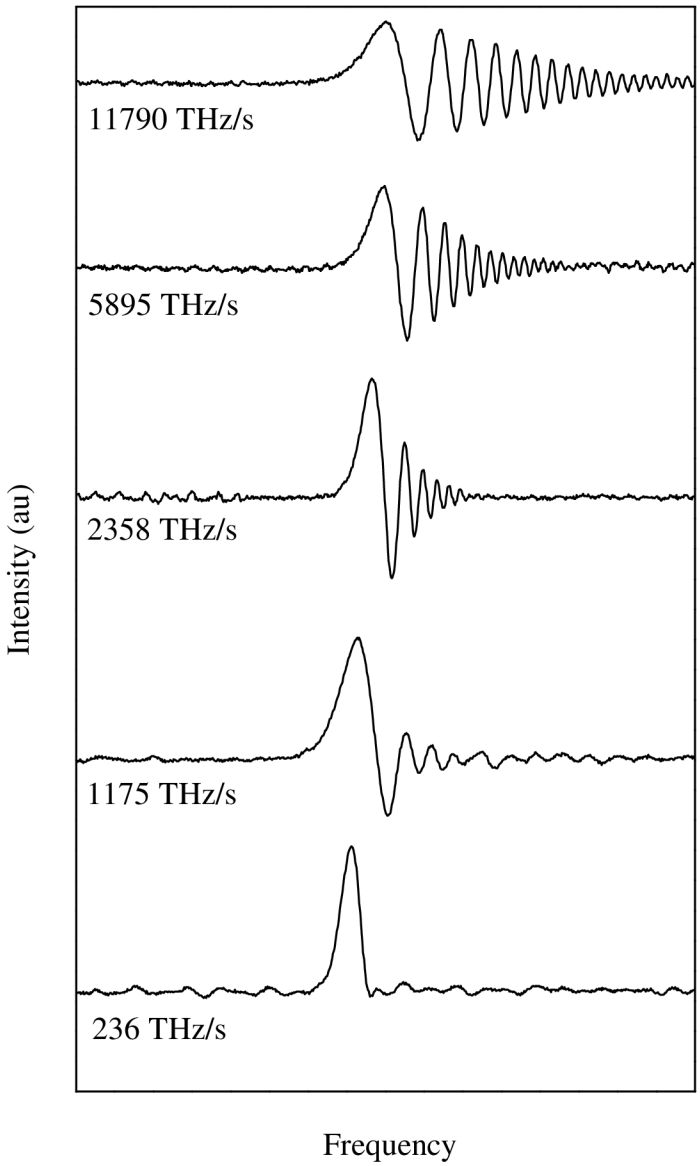

Figure 3.1: Depiction of transient effects distortion of spectra of BDPA with various sweeping rates. The lowest sweep rate in this figure, $b = 236\,\mathrm{THz/s}$, can still be considered slow enough to obtain slow passage spectrum. With increasing b the spectra get increasingly distorted by rapid-scan "wiggles".

3.2 Theory

In sec.2.3.2 the Bloch equations were derived and consequently their steady-state solution was presented (fig.2.5). This perfectly describes experiments, where the passage through

resonance is sufficiently slow to observe an absorption without any relaxation effects. However, in the case of rapid-scan the aim of the experiment is to attain a fast passage through resonance, which allows for observation of relaxation effects. To resolve the behaviour of the ensemble of spins theoretically, the Bloch equations have to be modified to accommodate the non-steady, rapid passage effects.

Furthermore, post-processing of the rapid-scan signal is usually employed to remove the distortion caused by rapid passage. For this purposes, the Fourier deconvolution is used, which in the end produces undistorted, slow-scan spectra.

3.2.1 Modified Bloch equations

The rapid-scan Fourier transform NMR[12], where the theoretical model explaining the rapid-scan phenomenon was described, takes into consideration only the linear system. The very same principles apply for rapid-scan EPR. Therefore, a modification of the Bloch equations (eq.(2.54)) is necessary so that its steady-state solution will be linearly proportional to the amplitude of the applied radiation. Writing Bloch equations in matrix form yields

$$\frac{\mathrm{d}\boldsymbol{M}}{\mathrm{dt}} = \begin{pmatrix} -1/T_2 & -\Omega_\mathrm{S} & 0 \\ \Omega_\mathrm{S} & -1/T_2 & \omega_1 \\ 0 & \omega_1' & -1/T_1 \end{pmatrix} \boldsymbol{M} - \begin{pmatrix} 0 \\ 0 \\ -M_0/T_1 \end{pmatrix} \tag{3.1}$$

where a distinction is made between ω_1 and ω_1' so that it can be decided which one should be neglected for the sake of the linearization. The steady-state solution is then

$$\boldsymbol{M} = \frac{M_0}{1 + (\Omega_\mathrm{S}T_2)^2 + \omega_1\omega_1'T_1T_2} \begin{pmatrix} \omega_1\Omega_\mathrm{S}T_2^2 \\ \omega_1 T_2 \\ 1 + (\Omega_\mathrm{S}T_2)^2 \end{pmatrix}. \tag{3.2}$$

The condition of linearization is the same as the condition of non-saturation (eq.(2.63))

$$\omega_1'\omega_1 T_1 T_2 \ll 1, \tag{3.3}$$

which is during the experiment achieved by attenuating the radiation amplitude. The solution from eq.(3.2) then reads

$$\boldsymbol{M} = \frac{M_0}{1 + (\Omega_\mathrm{S}T_2)^2} \begin{pmatrix} \omega_1\Omega_\mathrm{S}T_2^2 \\ \omega_1 T_2 \\ 1 + (\Omega_\mathrm{S}T_2)^2 \end{pmatrix}. \tag{3.4}$$

This shows that ω_1 cannot be neglected, otherwise only a trivial solution would be obtained. Since the difference between solutions in eq.(3.2) and eq.(3.4) is only a multiplicative factor, the first two homogeneous equations from eq.(3.2) can remain unchanged in the linearization. If we now neglect ω_1', we obtain

$$\frac{\mathrm{d}M_z}{\mathrm{dt}} = -\frac{1}{T_1}(M_z - M_0), \tag{3.5}$$

which provides only the solution $M_z = M_0$ as was predicted by eq.(3.4), so the differential equation for the z component degenerates to an algebraic equation $M_z - M_0 = 0$ and the Bloch equations can now be written as

$$\frac{\mathrm{d}}{\mathrm{dt}} \begin{pmatrix} M_x \\ M_y \end{pmatrix} = \begin{pmatrix} -1/T_2 & -\Omega_\mathrm{S} \\ \Omega_S & -1/T_2 \end{pmatrix} \begin{pmatrix} M_x \\ M_y \end{pmatrix} - \omega_1 \begin{pmatrix} 0 \\ M_0 \end{pmatrix}. \tag{3.6}$$

With introducing the complex notation $G = M_x + iM_y$ this leads to the well-known modified Bloch equation, first introduced by Jacobsohn and Wangsness[41] in 1948:

$$\frac{\mathrm{d}}{\mathrm{dt}}G = -\frac{1}{T_2}G + i\Omega_{\mathrm{S}}G - i\omega_1 M_0. \tag{3.7}$$

This equation was constructed under the approximation $M_z \approx M_0$, which also implies the linearization of the system.

In CW EPR experiments G is measured as a function of the frequency ($G = G(\omega)$) which is scanned with a constant velocity

$$\frac{\mathrm{d}\omega}{\mathrm{dt}} = b. \tag{3.8}$$

The magnitude of this velocity, also called "sweep rate", determines, whether the measurement is slow passage or rapid-scan. The dependence of spectral distortion due to varying b is depicted in fig.3.1. Thus it is obvious that there is no qualitative difference between these two kinds of measurements, if the measured spin system is linear.

With the relation

$$\frac{\mathrm{d}G}{\mathrm{dt}} = \frac{\mathrm{d}G}{\mathrm{d}\omega} \cdot \frac{\mathrm{d}\omega}{\mathrm{dt}} = b\frac{\mathrm{d}G}{\mathrm{d}\omega} = bG' \tag{3.9}$$

the modified Bloch equation (3.7) can be rewritten as

$$bG' = -\left(\frac{1}{T_2} - i\Omega_{\mathrm{S}}\right) G - i\omega_1 M_0, \tag{3.10}$$

which is the basic equation for rapid-scan EPR (and also rapid-scan Fourier transform NMR[12]).

It has been shown by Jen[12] that the solution to the modified Bloch equation is

$$G(\omega) = -i\omega_1 M_0 \int_0^\infty \exp\left(i\frac{b}{2}\tau^2 - \frac{1}{T_2}\tau + i\Omega_{\mathrm{S}}\tau\right) d\tau. \tag{3.11}$$

3.2.2 Processing the rapid-scan measurements

The procedure for obtaining the steady-state spectrum from a rapid-scan measurement with a constant sweep velocity b can be described in several steps. Since the rapid-scan spectrum is produced as a convolution of the response of the system (the steady-state solution) with the excitation, Fourier transform has to be applied with additional steps. The following solution was reported by Jen[12], other approaches are offered by Dadok[10] and Gupta[11].

The measured magnetization can be written as

$$M_b(\omega) = \frac{1}{2}\left[\exp(i\phi)G(\omega) + \exp(-i\phi)G^*(\omega)\right] \tag{3.12}$$

with the subscript b denoting rapid-scan and the asterisk denoting complex conjugate. The phase angle is assumed to be 0 for the dispersion measurement and $-\pi/2$ for the

absorption measurement; any deviation from these values means phase distortion.

The inverse Fourier transform of $M_b(\omega)$ is

$$m_b(t) = \frac{1}{2}\left[\exp(i\phi)g(t) + \exp(-i\phi)g^*(-t)\right] \tag{3.13}$$

where

$$\begin{aligned} g(t) &= \frac{1}{2\pi}\int_{-\infty}^{\infty} G(\omega)\exp(i\omega t)d\omega \\ &= -i\omega_1 M_0 \int_0^{\infty} \exp\left(i\frac{b}{2}\tau^2 - \frac{1}{T_2}\tau + i\omega_S\tau\right)d\tau \cdot \frac{1}{2\pi}\int_{-\infty}^{\infty}\exp\left[i\omega(t-\tau)\right]d\omega \\ &= -i\omega_1 M_0 \int_0^{\infty} \exp\left(i\frac{b}{2}\tau^2 - \frac{1}{T_2}\tau + i\omega_S\tau\right)\cdot\delta(t-\tau)d\tau \end{aligned} \tag{3.14}$$

from which we can see that for $t < 0$, $g(t) = 0$ and for $t > 0$ the $g(t)$ is

$$g(t) = -i\omega_1 M_0 \cdot \exp\left(i\frac{b}{2}t^2 - \frac{1}{T_2}t + i\omega_S t\right). \tag{3.15}$$

From this we can see that $g(t)$ is a so-called causal function, so we can easily separate the two terms in $m_b(t)$ from each other. The non-zero solution (for $t > 0$) will be denoted as $m_c(t)$ (as the result of causality)

$$m_c(t) = \frac{1}{2}\exp(i\phi)g(t). \tag{3.16}$$

The influence of rapid-scan can then be eliminated by dividing $m_c(t)$ with the excitation function $\exp(ibt^2/2)$:

$$m(t) = \frac{m_c(t)}{\exp(ibt^2/2)} = -\frac{i\omega_1 M_0}{2}\exp\left(i\phi - \frac{1}{T_2}t + i\omega_S t\right). \tag{3.17}$$

Finally, the Fourier transform back to the frequency domain yields

$$M(\omega) = \int_{-\infty}^{\infty} m(t)\exp(-i\omega t)dt = \frac{\exp(i\phi)}{2}\left(-\frac{i\omega_1 M_0}{1/T_2 - i\Omega_S}\right). \tag{3.18}$$

The expression in brackets is exactly the steady-state solution as we can see from eq.(3.10) while the multiplier is a constant for correct phase angle or a phase distortion in general. Both absorption and dispersion spectra can be thus obtained.

4 Experimental details

This chapter is split into two parts. The first, sec.4.1, describes the home-built spectrometer used to conduct the rapid-scan experiments. The second part, sec.4.2, describes how the experiment was prepared and conducted, including the samples and the experimental procedure.

4.1 Home-built HFEPR spectrometer

The first combined Terahertz Field and Frequency Domain Electron Paramagnetic Resonance (HFEPR/FDMR) spectrometer[23], built at the University of Stuttgart, was designed to investigate the electronic structure and magnetic properties of molecular systems, thin films and solid state materials in a very broad frequency range (85-1100 GHz). Common EPR spectrometers are usually operated at fixed microwave frequencies of 10 GHz (X-band) and magnetic field of approximately 0.3 T (considering the free electron g-value of 2). However, high fields and frequencies lead to dramatic increase of sensitivity. The advantage of HFEPR also lies in the delivery of higher g-value resolution, which allows establishing the electronic and geometric structures of examined materials (e.g. active centers in enzymes[42]). High frequencies also give access to large energy gaps, as in the case of a large zero-field splitting.

This spectrometer was slightly modified from its usual setup described by Neugebauer[23] for the reasons of rapid-scan measurements, the difference being the microwave source, detector and readout, as described in the following sections. No modification was made to the quasi-optical table nor the magnet.

Source

As a source of microwaves a voltage-controlled oscillator (VCO; VO4280X/00, manufactured by Sivers IMA), operating in range 3 to 20 GHz, was used. The offset voltage V_0 was provided by a laboratory power source of high stability. The modulation voltage, which was converted to the sweeping microwaves by the VCO, was provided by a lock-in amplifier (Zurich Instruments MFLI Lock-in Amplifier). These two voltages were mixed by a Bias-Tee module (ZFBT-6GW+; manufactured by Mini-Circuits) before being introduced to the VCO. The microwaves from the VCO were then introduced to a WR9.0 Amplifier / Multiplier Chain (AMC; manufactured by Virginia Diodes, Inc.), which multiplied the frequency by a factor of 18 to reach the desired frequency range for the experiment (170 - 250 GHz); this is depicted in fig.4.2, the experimentally determined dependence of frequency of microwaves produced by the VCO on introduced voltage is shown in fig.4.3.

Magnet

The sample was located in the center of a superconducting solenoid, cooled with liquid He, with can produce magnetic fields up to 17 T. The magnet was equipped with Variable Temperature Insert (VTI) cryostat with an inner diameter of 30 mm, both from Oxford

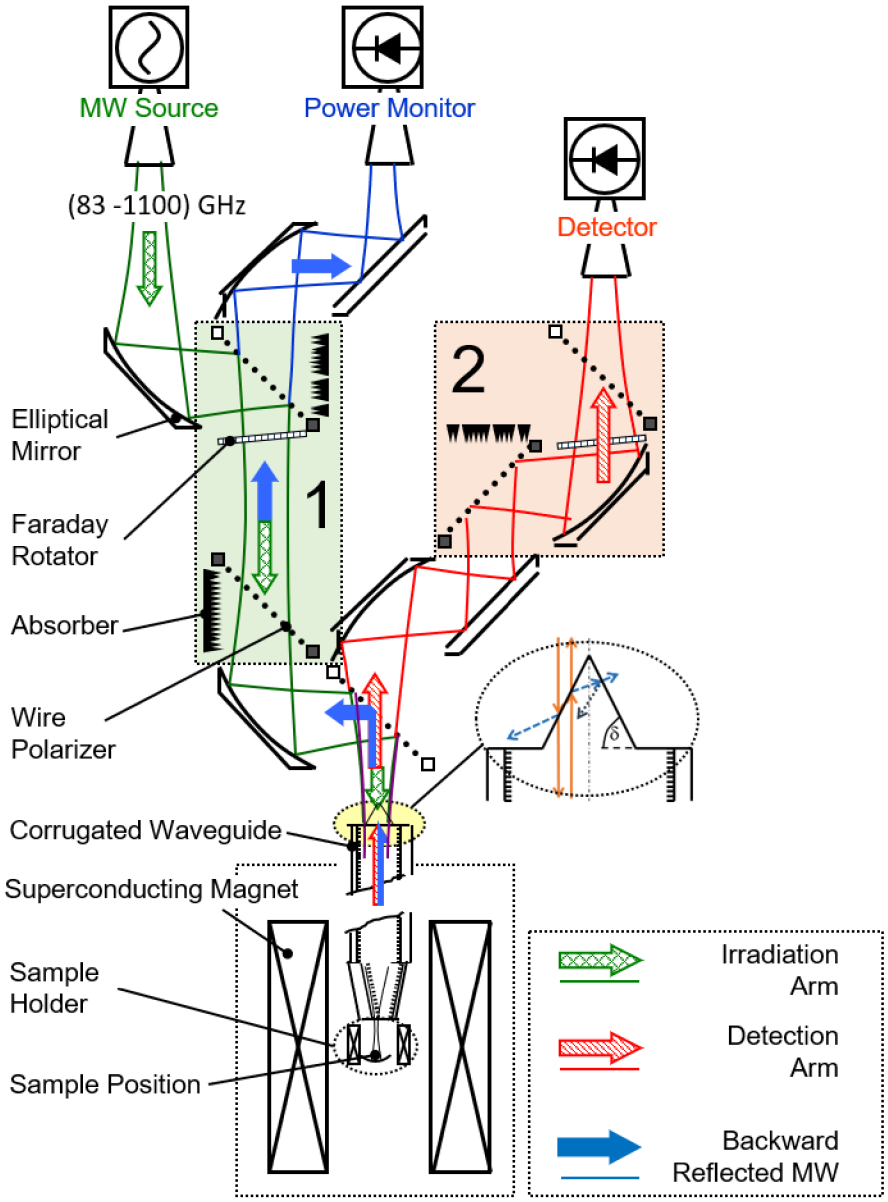

Figure 4.1: A schematic description of the home-built spectrometer[23] at the University of Stuttgart. This spectrometer is equipped with a quasi-optical bridge, in this figure separated into the reference arm (1) and the detection arm (2). The superconducting magnet is cooled by liquid He. Courtesy of Dr. Neugebauer.[23]

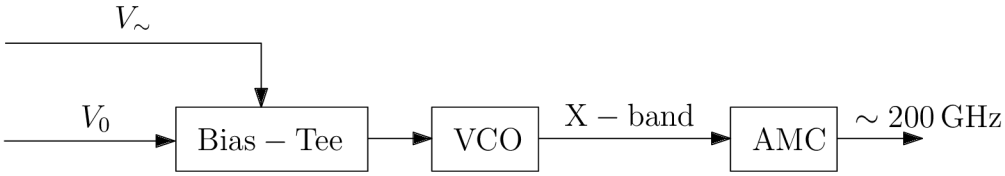

Figure 4.2: A schematic depiction if the microwave source. Offset voltage V_0 is mixed with modulation voltage $V_\sim$ in the Bias-Tee module, then converted into microwaves by the VCO and multiplied by AMC to reach desired frequency range.

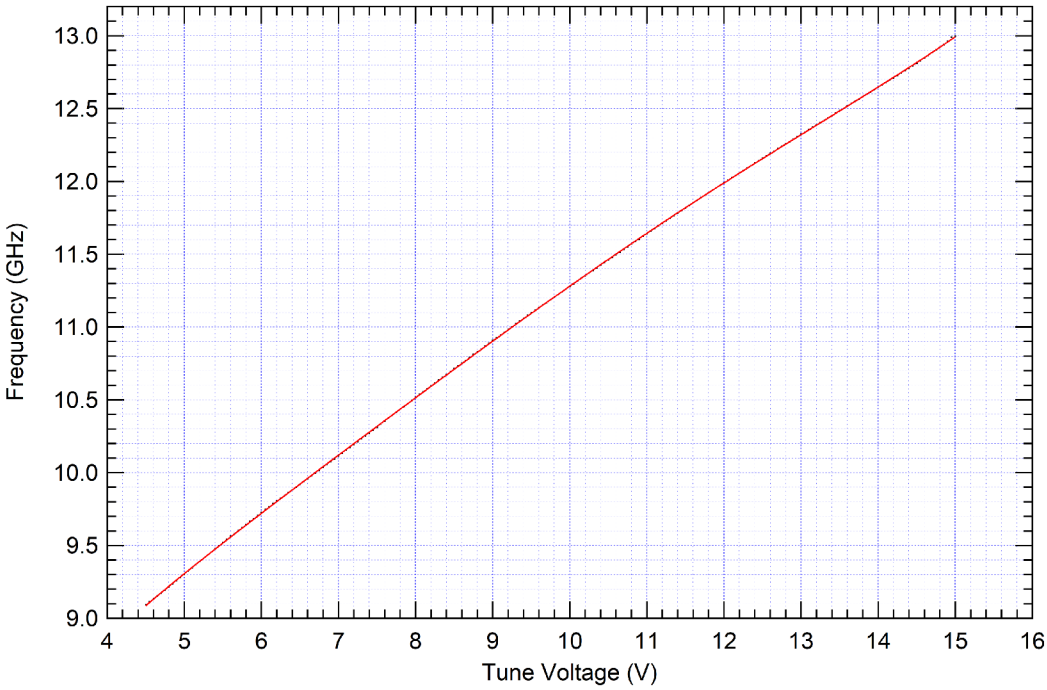

Figure 4.3: Dependence of microwave frequency produced by the VCO on the introduced voltage. Courtesy of Dr. Laguta.

Instrumets Ltd. The maximum sweep rate of the magnet was 1 T/min and the VTI allowed the temperature control in the range from 1.6 K to 300 K.

Wave propagation

To propagate the microwaves, a low loss quasi-optical bridge and a corrugated waveguide was used (see fig.4.1). Outside the cryostat the microwaves were propagated as free space linearly polarized Gaussian beam between broadband off-axial quasi-optical components, arranged on a quasi-optical table. Inside the cryostat, a low loss oversized corrugated waveguide optimized for 315 GHz or 630 GHz was used for propagating the microwaves in the HE_{11} mode[23]. The quasi-optical table was placed on a movable stand allowing loading of the sample rod into the cryomagnet as well as horizontal, vertical and angular alignment of the quasi-optical bridge. The alignment was done by micrometric screws allowing fine tuning of the microwave coupling to the waveguide.

The microwave from the source was coupled to the quasi-optical bridge by dedicated corrugated horns for a given frequency band. Afterwards it was propagated in free space on the quasi-optical table hitting the first off-axial mirror, which was used to defocus the divergent Gaussian beam (microwave is refocused every 250 mm). The beam was then reflected by a vertical wire grid polarizer, defining a linear polarization, transmitted through an exchangeable Faraday rotator, which rotated the polarization by 45°. It then passed through 45° wire polarizer, which in combination with the previous vertical grid and Faraday rotator formed a quasi-optical circulator. After that it was again refocused by elliptical mirror, reflected by a wire grid polarizer and coupled into a 1.8 m long, 18 mm inner diameter corrugated waveguide, which was used to propagate the wave inside a cryostat.

Detection and readout

The linearly polarized microwave (green arrow in fig.4.1) upon interaction with the sample was reflected back either by a golden mirror underneath the sample or by the sample itself. The microwave then returned to the quasi-optical bridge. In case of resonance, the returning microwave was no longer linearly polarized, because one of the circular radiation components interacted more strongly with the sample than the other. The polarizer above the cryostat thus split the signal into co-polar and cross-polar signals. Usually, the detector was placed so it detected the cross-polar signal, since in common CW experiments the absorption signal is stronger in the cross-polar arm (red in fig.4.1); however, during our rapid-scan experiments it proved more effective to detect the absorption signal in the co-polar arm (blue in fig.4.1) since the overall signal was stronger in this arm, at the cost of intensive standing waves.

A zero-biased Schottky diode (WR4.3ZBD-F 170-260 GHz manufactured by Virginia Diodes, Inc.) was used as a fast detector (up to 36 GHz bandwidth). The signal from the detector was read out and digitized by DSOS604A High-Definition Oscilloscope (6 GHz, 4 analog channels; manufactured by Keysight Technologies, Inc.). The source of the modulation signal (MFLI Lock-in amplifier from Zurich Instruments) generated the trigger signal for averaging as well.

4.2 Description of experiment

Generally, the resonance signal is always mixed with the background standing waves in the optical path. Usually, the signal is not visible by naked eye (with the exception of several samples with a very intensive signal, such as in fig.4.4), therefore the background (or the "reference signal") had to be subtracted from the acquired signal (background with resonance signal). This was done by first setting the microwaves into desired core frequency with desired sweep (and by that managing that the standing waves in the system would be the same for the length of the experiment), letting the temperature stabilize, setting the magnetic field just so that the resonance signal would not be detected and then collecting the off-resonance reference signal, which would later be numerically subtracted from the on-resonance signal. Defining "on-resonance" and "off-resonance" signals was possible since the g-values of examined molecules are well known and it is therefore easy to calculate the resonance position from the resonance condition (2.10).

4.2.1 Samples

Two organic radical samples were examined – BDPA and LiPc. These were chosen for their very narrow linewidth and relative availability. Their detailed description follows in the next paragraphs.

BDPA

The abbreviation "BDPA" is used here for α,γ-Bisdiphenylene-β-phenylallyl complex with benzene (1:1), as shown in fig.4.5. BDPA is a promising DNP agent[24,25]. The sample

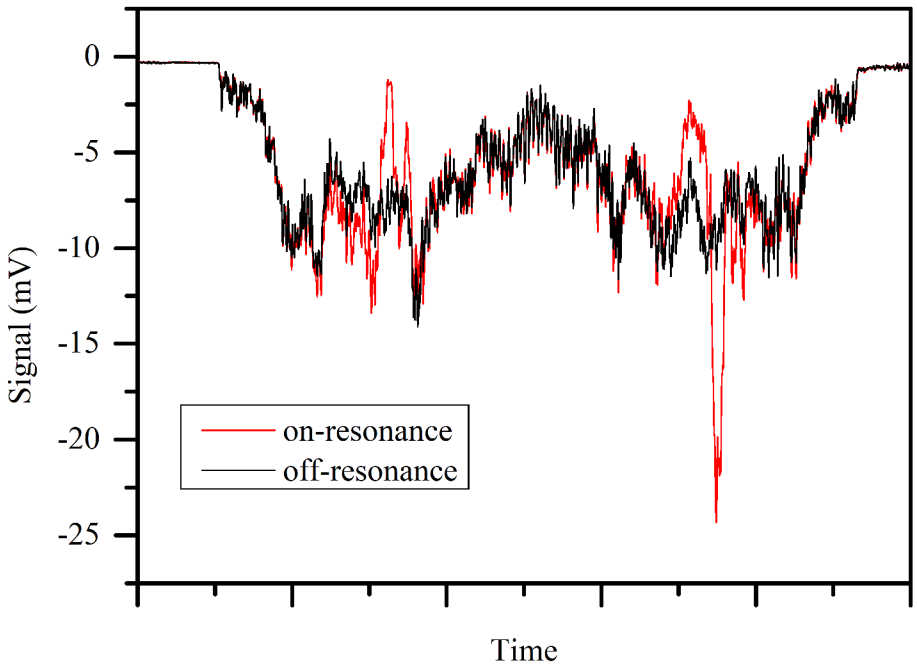

Figure 4.4: Comparison of on- and off-resonance signals with chirp pulses produced by a Keysight Arbitrary Waveform Generator; additionally, these sweeps were linear. Measured on BDPA sample at 15 K with direct detection, sweep duration of 20 ns (this sweep was 5 times faster than the VCO is able to produce), 4069 averages (total acquisition time being approx. 164 s). This is an unusually strong resonance signal.

itself was prepared by dissolving solid polystyrene in toluene solution of BDPA, provided by Sigma-Aldrich. Out of the resulting highly viscous solution small drops (roughly 3 mm in diameter) were put on a watch glass and left under a fume hood until the toluene completely evaporated from the droplets. The resulting flat, round-shaped thin foils were a solid solution of BDPA-benzene complex and polystyrene, in concentration of 10 mM.

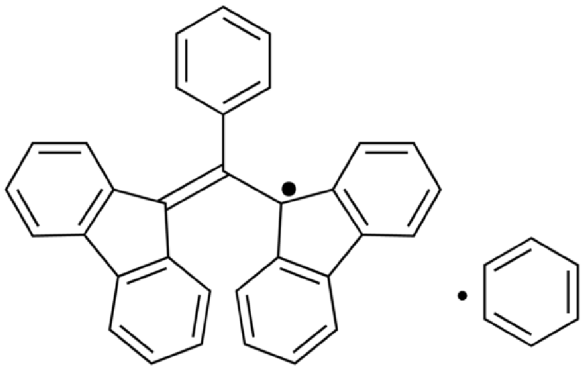

Figure 4.5: α,γ-Bisdiphenylene-β-phenylallyl complex with benzene (1:1), abbreviated as BDPA.

LiPc

The "LiPc" abbreviation stands for the lithium-phthalocyanine radical (see fig.4.6). Small crystals of it, synthesized at the University of Stuttgart, were ground to a fine powder, wrapped into teflon and pressed into a 2 mg pellet.

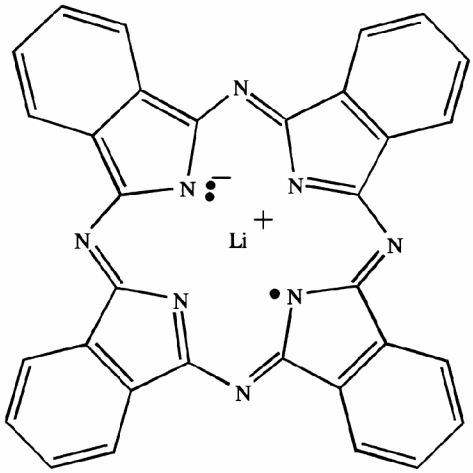

Figure 4.6: Lithium phthalocyanine radical, abbreviated as LiPc.

5 Results

Before the present work the rapid-scan EPR was demonstrated only at frequencies below 100 GHz[16]. Here in sec.5.1 we present historically first observations made upon two organic radical samples (sec.4.2.1) at frequencies around 200 GHz with various sweeping rates – this is in fact the very first multi-frequency rapid-scan experiment ever reported. All spectra shown here are after subtraction of background.

Subsequently in sec.5.2, we explain an algorithm for extracting the steady-state spectra from the rapid-scan data and their comparison to measured slow-scan spectra. Furthermore, in this section the numerical solution of Bloch equations (using the native MATLAB function *ode45*) with rapid frequency sweeps is employed to obtain a reasonable estimation of the relaxation time T_2 by comparing the calculated spectra with the measured ones.

5.1 Rapid-scan experiment

The frequency was rapidly swept through resonance in sinusoidal sweeps, as depicted in fig.5.1, during every measurement. Each sweep was than characterized by the offset frequency ω_{off}, amplitude of sweep A_ω, sweep frequency f_ω and risetime t_ω (sweep frequency and risetime were related as $t_\omega = f_\omega^{-1}/2$). Each spectrum was averaged 4096 times.

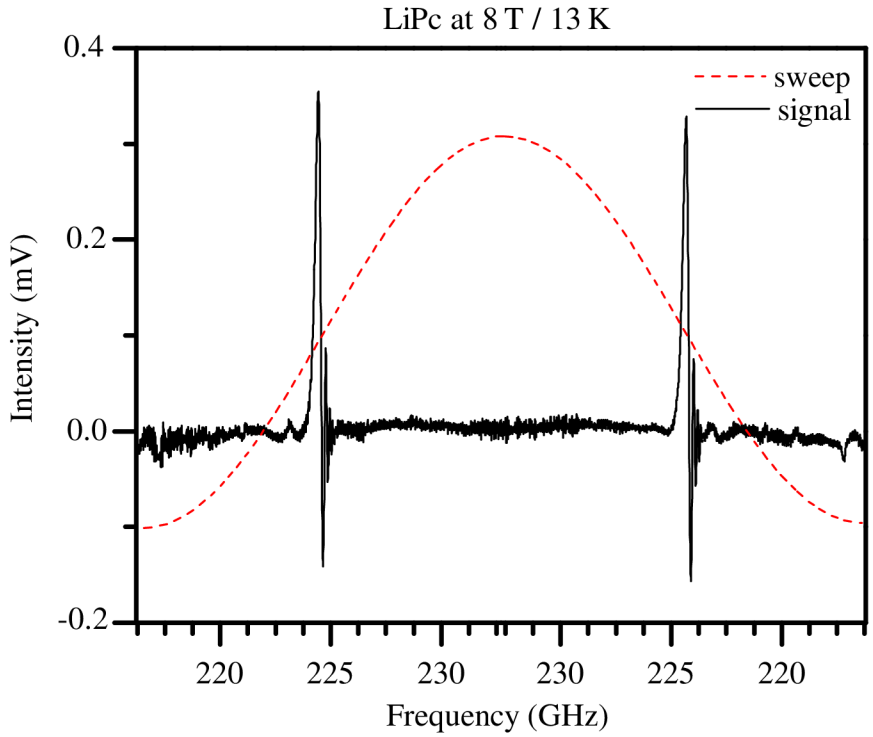

Figure 5.1: Resonance signal during sinusoidal frequency sweeping up and down, from LiPc sample at 8 T and 13 K. The frequency of sweeps was $f_\omega = 2$ MHz with central frequency set at $\omega_{\text{off}} = 224.7$ GHz and sweep amplitude $A_\omega = 8$ GHz.

Out of the varying amplitude A_ω and sweep frequency f_ω a maximum sweep rate at the center of the sweep could be calculated for each spectrum as

$$b_{\max} = A_\omega f_\omega. \tag{5.1}$$

Fig.5.2 shows increasing distortion of LiPc absorption spectrum (the bottommost spectrum can still be considered a slow-scan spectrum) with increasing sweep rate b. The same principle is illustrated at different field-frequency combination in fig.5.3. The same phenomenon is observable in BDPA spectra (fig.5.4 and 5.5), although with this sample the rapid passage distortion occurs at lower sweeping rates, which hints a higher value of T_2. Also the difference in line width between LiPc and BDPA is apparent.

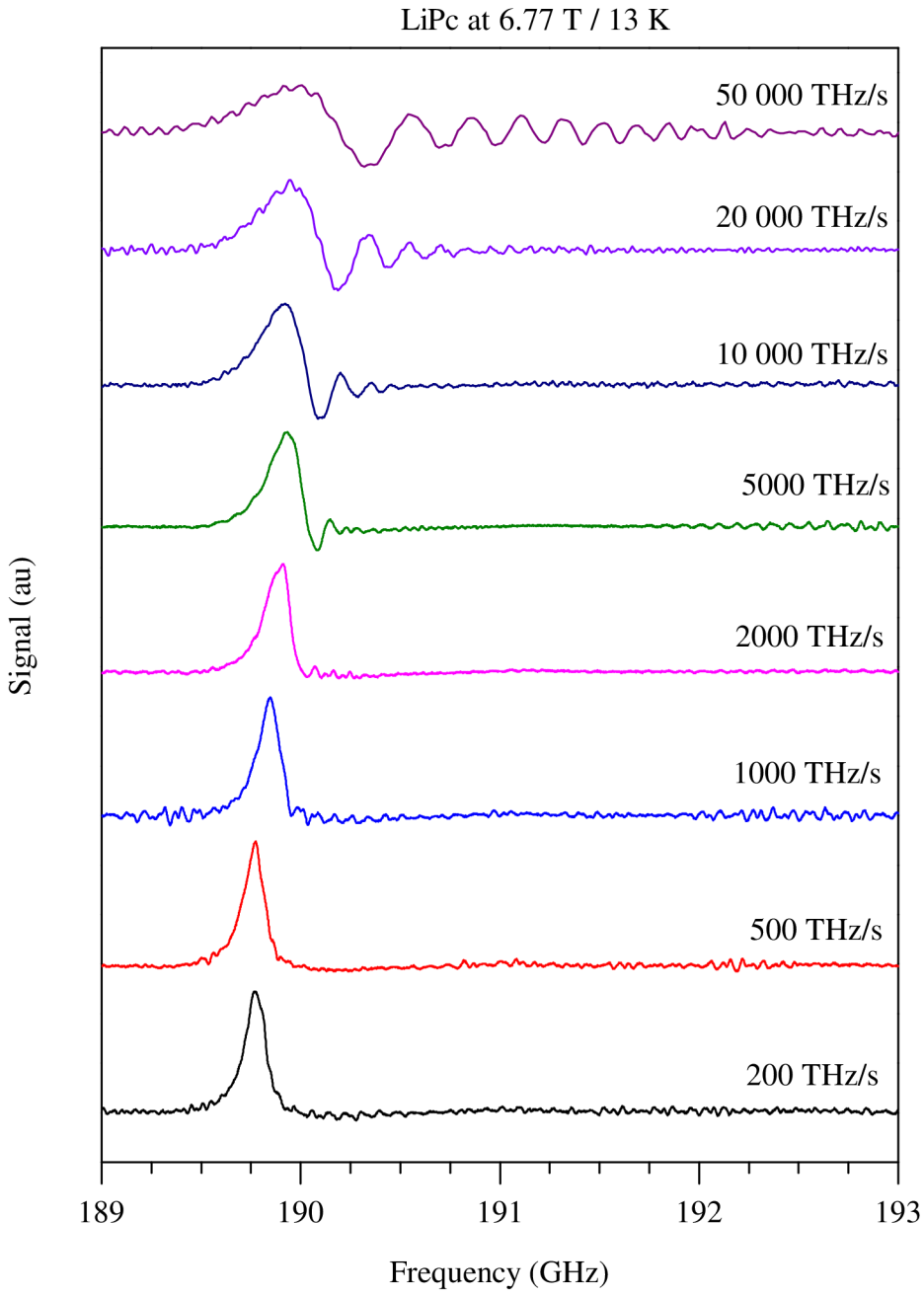

Figure 5.2: Resonance signal of LiPc sample at 6.77 T and 13 K at various sweeping rates. Frequency offset was set to $\omega_{\text{off}} = 190.4\,\text{GHz}$ and sweep amplitude to $A_\omega = 10\,\text{GHz}$. Maximum sweeping rate employed for this measurement was 50 000 THz/s, during which the observed spectrum became too noisy. The spectrum with lowest sweeping rate, $b = 200\,\text{THz/s}$, can still be considered a slow-scan spectrum. 4096 averages.

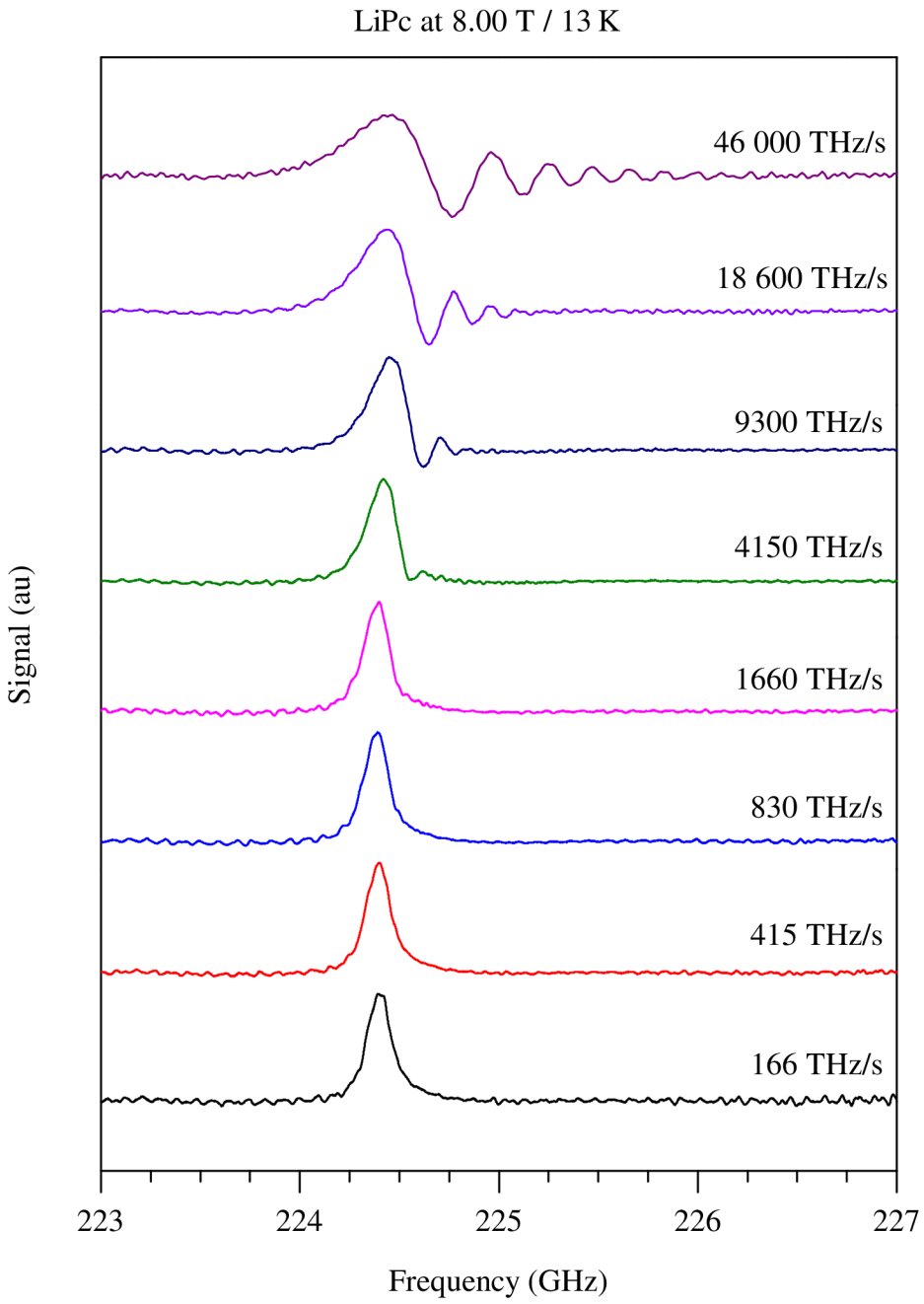

Figure 5.3: Resonance signal of LiPc sample at 8.00 T and 13 K at various sweeping rates. Frequency offset was set to $\omega_{\text{off}} = 225.0\,\text{GHz}$ and sweep amplitude to $A_\omega = 8.3\,\text{GHz}$. Maximum sweeping rate employed for this measurement was 46 000 THz/s. A slight peak distortion can be observed as low as at 4150 THz/s sweep rate. 4096 averages.

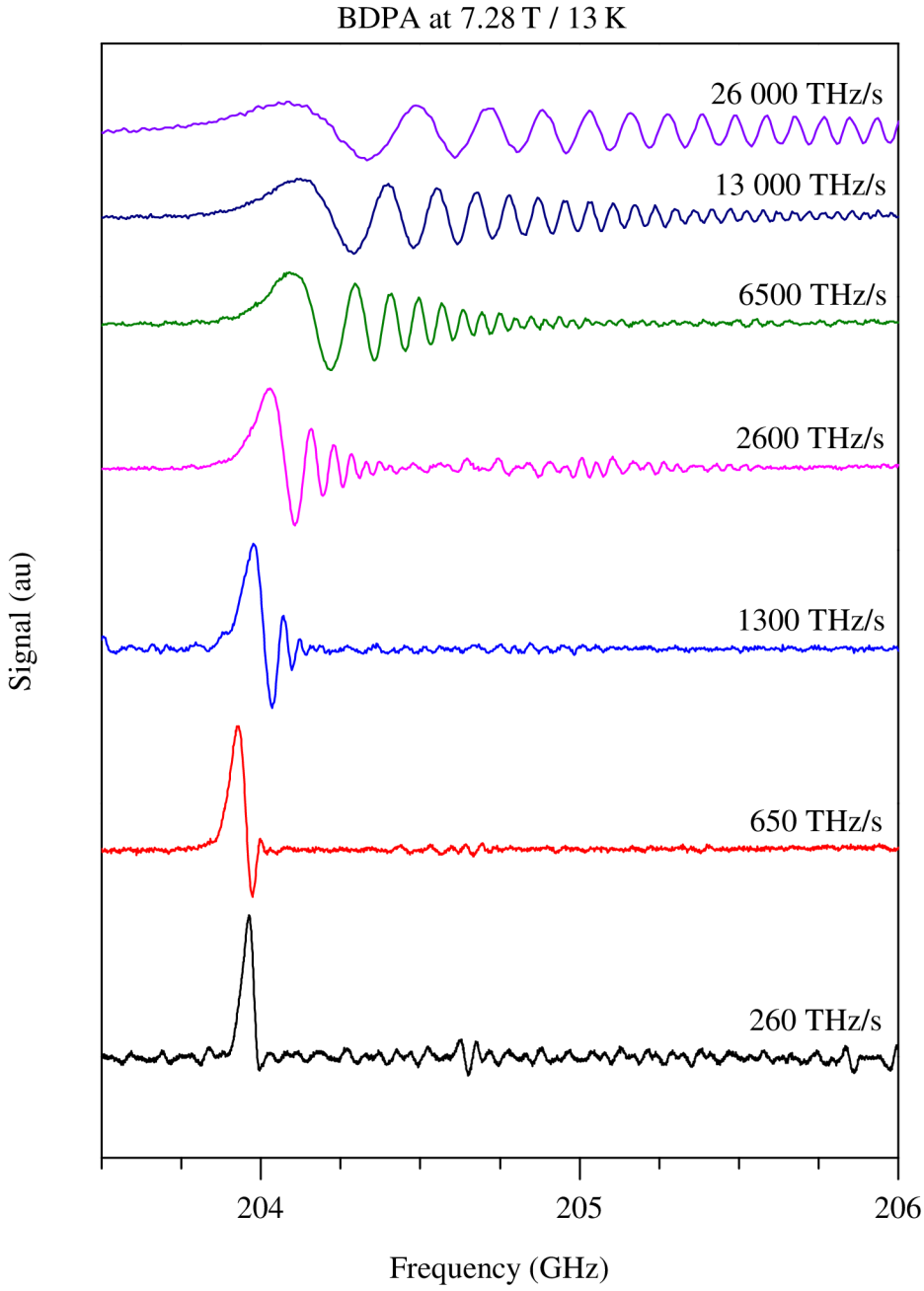

Figure 5.4: Resonance signal of BDPA sample at 7.25 T and 13 K at various sweeping rates. Frequency offset was set to $\omega_{\text{off}} = 204.4\,\text{GHz}$ and sweep amplitude to $A_\omega = 13.0\,\text{GHz}$. Maximum sweeping rate employed for this measurement was 26 000 THz/s. 4096 averages.

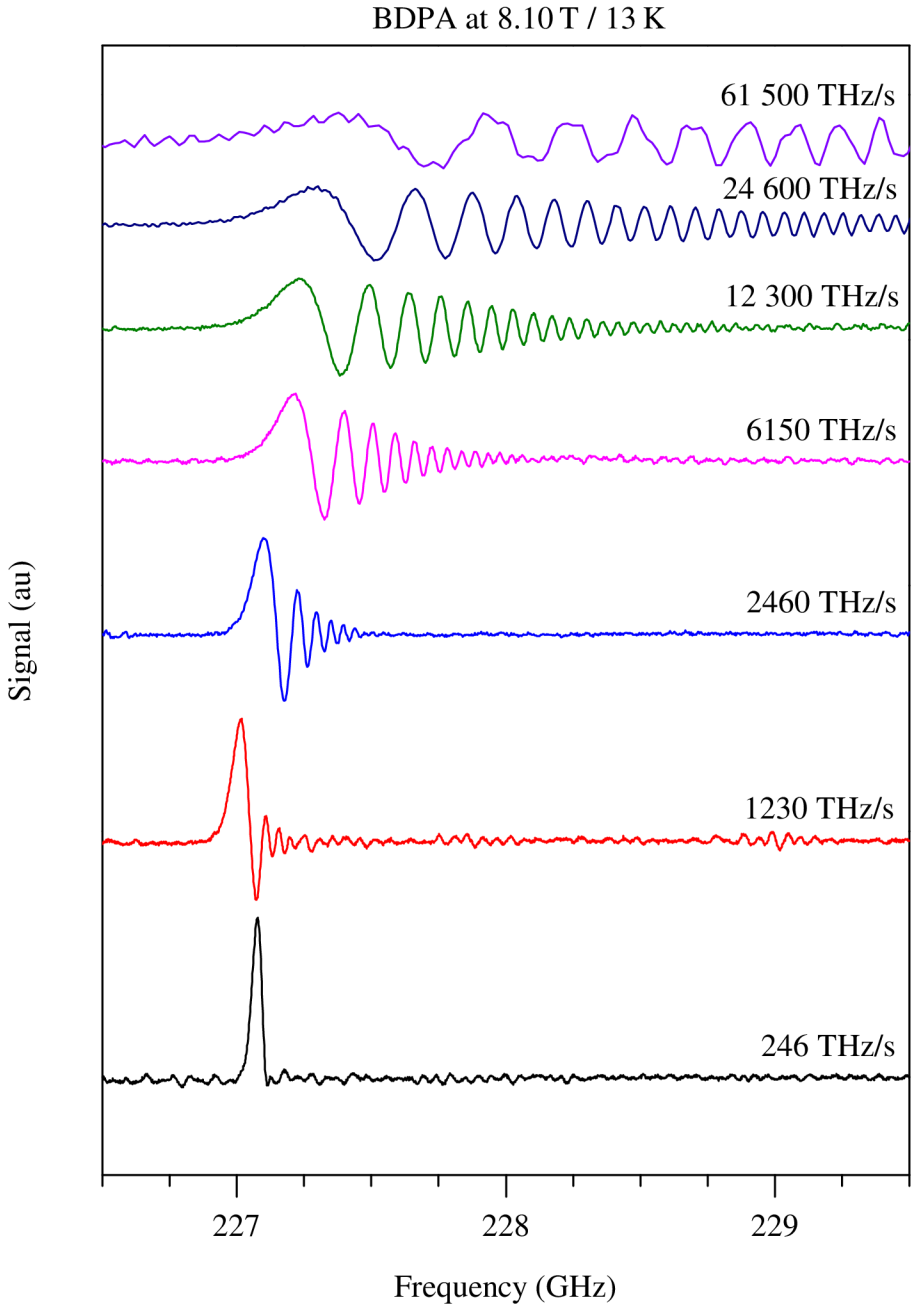

Figure 5.5: Resonance signal of BDPA sample at 8.10 T and 13 K at various sweeping rates. Frequency offset was set to $\omega_{\text{off}} = 227.4\,\text{GHz}$ and sweep amplitude to $A_\omega = 11.8\,\text{GHz}$. Maximum sweeping rate employed for this measurement was 61 500 THz/s. Due to the oscilloscope's limited number of samples per unit of time, the spectrum swept at highest rate exhibits high noise distortion. 4096 averages.

5.2 Data processing

This section is divided into two parts: in the first part we describe a process of extracting the slow-scan from the rapid-scan spectra by means of Fourier deconvolution. In the second we extract information about T_2 from the rapid-scan spectra by numerically solving Bloch equations in MATLAB (using the native function *ode45*) with variable T_2, while comparing the spectrum with the numerical solution to determine the best fit.

5.2.1 Fourier deconvolution

Here we present an algorithm to process the data distorted by rapid passage through resonance. The theoretical description can be found in sec.3.2.2. Every frequency offset was set in such a way that the resonance occurred in the middle of the sweep; that allowed us to approximate the sinusoidal sweep as linear for the width of the spectrum, therefore we could have created an analytical function in the shape of a complex exponential with a linear increase of frequency as the excitation.

We consider the measured spectra as a frequency domain data. It can be written as

$$M(\omega) = R(\omega) * E(\omega), \tag{5.2}$$

where $M(\omega)$ is the measured spectrum, $R(\omega)$ is the response of a linear system and $E(\omega)$ is the excitation function. As this equation describes, the slow scan spectrum $R(\omega)$ becomes convoluted with the microwave excitation $E(\omega)$ to yield the rapid-scan spectrum $M(\omega)$.

To obtain the slow scan spectrum $R(\omega)$ (the usual product of CW experiment), we first had to apply inverse Fourier Transform, the result being

$$m(t) = r(t)e(t). \tag{5.3}$$

Here the convolution became a simple multiplication and $r(t)$ denotes the response in time domain. Had the excitation $e(t)$ been a short pulse, the measured spectrum $m(t)$ would be the free induction decay, the usual product of pulsed techniques.

The excitation $e(t)$ for linearly increasing frequency of microwave radiation can be analytically expressed as

$$e(t) = \exp\left(i\frac{bt^2}{2}\right), \tag{5.4}$$

where t stands for the time variable. We could then divide the time-domain spectrum with the excitation function to obtain the time-domain response,

$$\frac{m(t)}{e(t)} = \frac{m(t)}{\exp(ibt^2/2)} = r(t). \tag{5.5}$$

Consequently, we applied Fourier Transformation to obtain the deconvoluted frequency-domain response $R(\omega)$. This simple algorithm is schematically depicted in fig.5.6, the corresponding spectra in individual steps are depicted in fig.5.7 (similarly to Dadok[10]).

Home-written script in MATLAB was used to process the rapid-scan spectra. Since a direct detection, that means one channel with no phase sensitivity, was used, the input

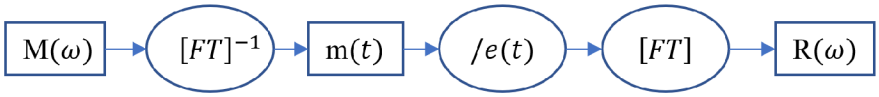

Figure 5.6: Schematic depiction of the deconvolution algorithm used to obtain undistorted slow scan spectra.

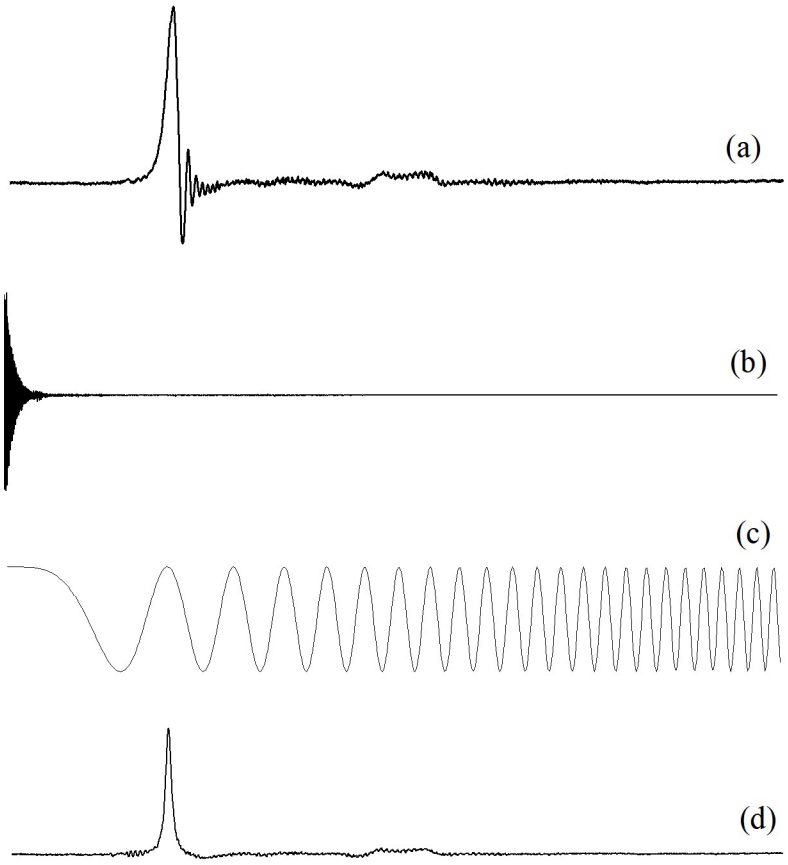

Figure 5.7: Schematic depiction of the spectra during the deconvolution algorithm, used to obtain undistorted slow scan spectra. (a) The measured rapid-scan spectrum (arbitrary), (b) inverse Fourier Transform of the rapid-scan spectrum. The mirror image produced by the transformation was manually set to zero. (c) Excitation function. (d) Deconvoluted spectrum. In (b-d) only the real parts are shown.

into the deconvolution script was purely real. Therefore, after the deconvolution process, only the real part of the outcome was used to display the results.
Out of here reported rapid-scan spectra a few have been chosen to demonstrate our ability to extract a slow scan spectrum. Two LiPc and two BDPA spectra have been chosen.

Fig.5.8 shows rapid-scan spectrum (black) of LiPc at 6.33 T while sweeping 10 000 THz/s. The subsequently deconvoluted spectrum (red) is in a good accord with the slow-scan spectrum (blue) obtained by sweeping 200 THz/s at the same field (at this rate it can still be

considered a slow-scan spectrum; see fig.5.2). Fig.5.9 shows rapid-scan spectrum (black) of LiPc at 8.00 T while sweeping 18 600 THz/s and subsequently deconvoluted spectrum (red) overlapping with a slow-scan spectrum (blue) obtained by sweeping 166 THz/s at the same field (this rate can also be considered too low for distorting the LiPc spectra. See fig.5.3).

The imperfection of overlapping and slight asymmetry of the deconvoluted and slow-scan peaks is most likely caused by approximating a center of sinusoidal sweep as linear.

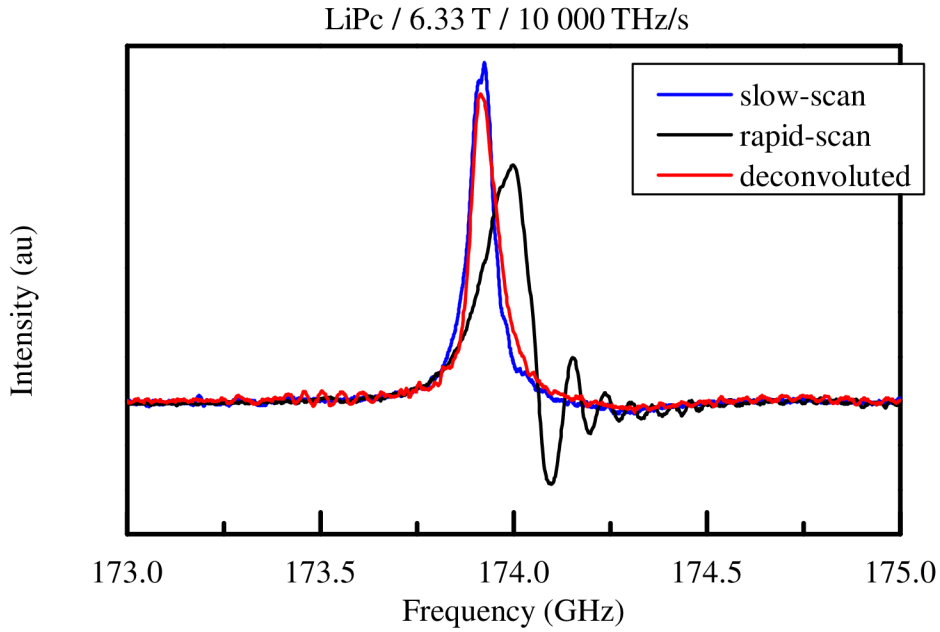

Figure 5.8: Experimental (black), deconvoluted (red) and slow-scan (blue) spectra of LiPc at 6.33 T. Rapid-scan spectrum was obtained while sweeping 10 000 THz/s. The imperfection of the overlapping of the deconvoluted and slow-scan spectra is most probably caused by non-linearity of the sinusoidal sweep..

Fig.5.10 shows rapid-scan (black), slow-scan (blue) and deconvoluted (red) spectrum of BDPA at 7.28 T. The rapid-scan spectrum was obtained while sweeping 13 000 THz/s. The asymmetry of the deconvoluted and slow-scan peak and their imperfect overlapping is caused by undesirable attenuation of the rapid-scan signal, that causes the decay of the "wiggles" to be apparently linear; another reasons for these imperfections are approximating the sinusoidal sweep as linear and detecting a mixture of absorption and dispersion. As the slow-scan spectrum the one measured with the lowest sweep rate (260 THz/s in fig.5.4) was used.

Fig.5.11 shows rapid-scan (black), slow-scan (blue) and deconvoluted (red) spectrum of BDPA at 8.10 T. The rapid-scan spectrum was obtained while sweeping 2460 THz/s. The asymmetry of the deconvoluted peak is caused by undesirable attenuation fo the rapid-scan signal. Mixture of absorption and dispersion is another possible explanation. As the slow-scan spectrum the one measured with the lowest sweep rate (246 THz/s in fig.5.5) was used.

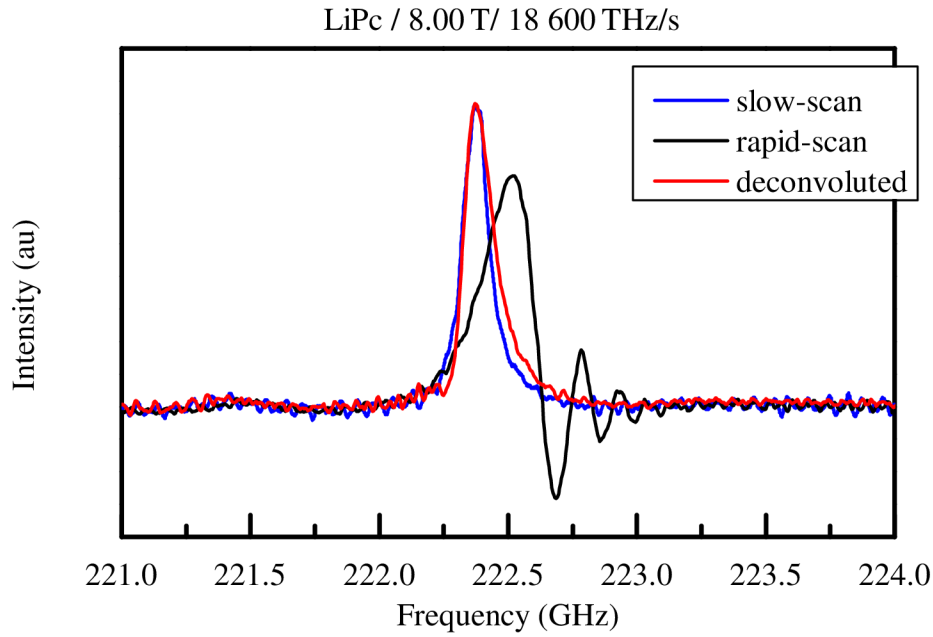

Figure 5.9: Experimental (black), deconvoluted (red) and slow-scan (blue) spectra of LiPc at 8.00 T. Rapid-scan spectrum was obtained while sweeping 18 600 THz/s.

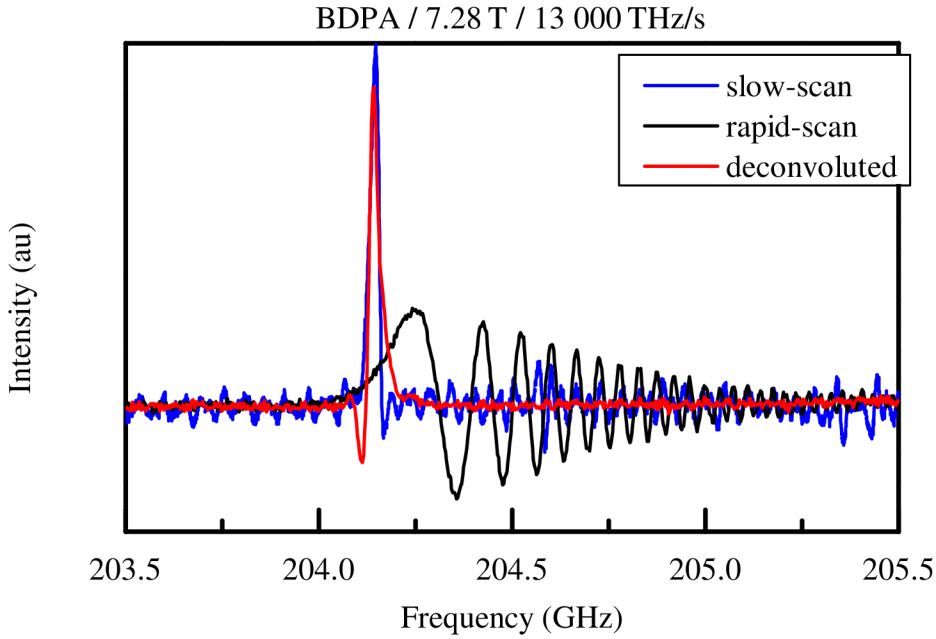

Figure 5.10: Experimental (black), deconvoluted (red) and slow-scan (blue) spectra of BDPA at 7.28 T. Rapid-scan spectrum was obtained while sweeping 13 000 THz/s. The undesirable attenuation of the rapid-scan signal is clearly visible; this is also causing the severe asymmetry of the deconvoluted peak.

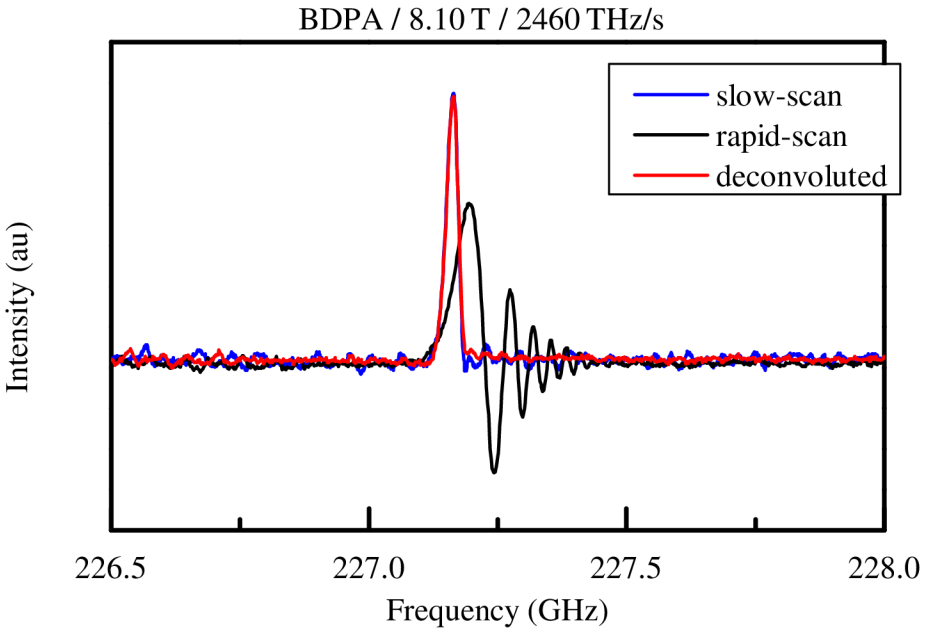

Figure 5.11: Experimental (black), deconvoluted (red) and slow-scan (blue) spectra of BDPA at 8.10 T. Rapid-scan spectrum was obtained while sweeping 2460 THz/s.

There is a noticeable shift in the resonance peak between the figures with deconvoluted spectra (fig.5.8 - 5.11) and those with raw rapid-scan spectra (fig.5.2 - 5.5) – the raw data are plotted against the experimental, sinusoidally increasing, values of frequency, whereas the deconvoluted spectra are plotted against a linearly increasing frequency obtained by approximating the sinusoidal sweep as linear. It was not possible to work only with a narrow band of frequencies in the center of the sweep, which would yield lesser shift when approximated, since we had to maintain a sufficient number of points for the discrete Fourier transformation.

5.2.2 Calculations

In order to extract the T_2 value, the Bloch equations had to be numerically solved (using MATLAB native function *ode45*) for rapid frequency sinusoidal sweeps. T_2 was then manually tuned in order to obtain spectra of sufficient similarity to the measured one. Fig.5.12 shows this process with a BDPA spectrum measured at 8.10 T while sweeping 2460 THz/s. The resulting value of the relaxation time for a sufficiently overlapping spectrum was $T_2 = (50 \pm 10)$ ns. Fig.5.13 shows the same process with a LiPc spectrum measured at 8.00 T while sweeping 46 000 THz/s; the resulting value of the relaxation time was $T_2 = (12 \pm 2)$ ns.

This difference is best depicted by the fact that to obtain a similar number of wiggles, the sweep rate for LiPc (which has considerably lower T_2) had to be almost 20 times higher than that used for obtaining the BDPA spectrum.

The value of T_2 relaxation time reported by Meyer [43] and Stoner [37] (2.5 µs for LiPc and 6 µs for BDPA) differ significantly from our results; however, given that the relaxation times strongly depend on molecular environment and frequency offset, this is not

very surprising.

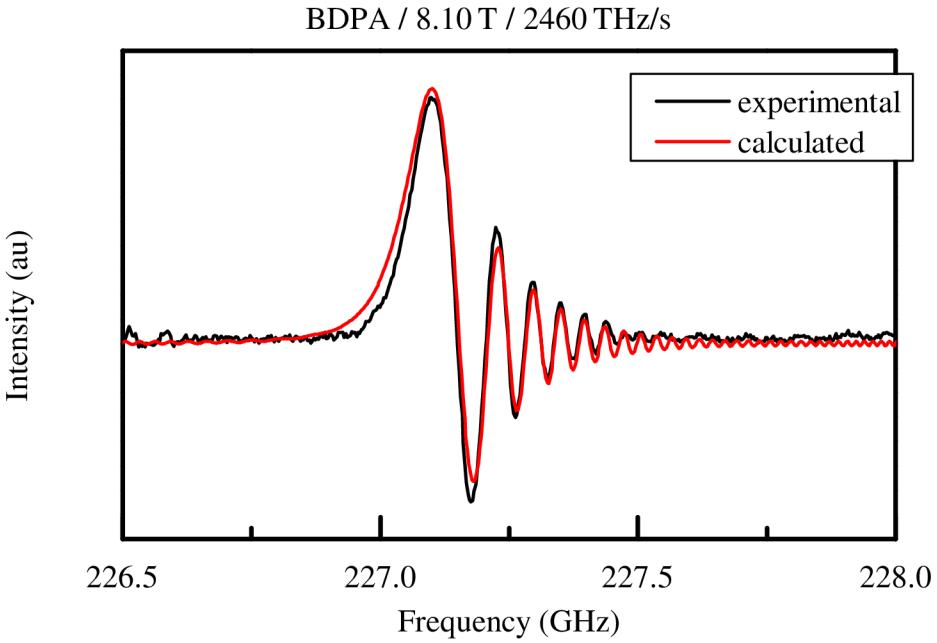

Figure 5.12: Rapid-scan spectrum of BDPA at 8.10 T and sweep rate 2460 THz/s (black) and spectrum calculated by numerically solving Blochquations with variable T_2 (red). The resulting value was $T_2 = (50 \pm 10)$ ns.

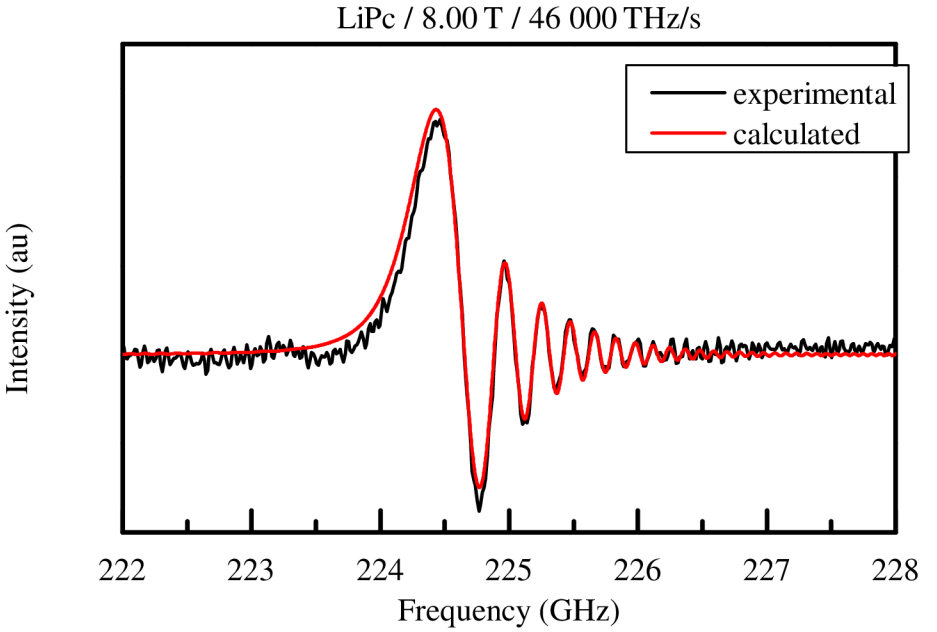

Figure 5.13: Rapid-scan spectrum of LiPc at 8.00 T and sweep rate 46 000 THz/s (black) and spectrum calculated by numerically solving Bloch equations with variable T_2 (red). The resulting value was $T_2 = (12 \pm 2)$ ns.

Since a direct detection was used (see sec.4.2 for more details), we were not able to separate absorption and dispersion signals. It is thus highly unlikely that, even though the observed spectra resemble pure absorption (as described by Hyde[16]), the two signals are not mixed in an unknown ratio. Therefore, while the calculations were approached as though pure absorption was detected, the probable mixture of absorption and dispersion signals is most likely responsible for the imperfection of the overlapping.

This method of overlapping measured and calculated spectra is rather crude; however, it serves well to obtain a reliable estimate of the T_2 relaxation time in a short amount of time. This is by no means intended as a high-end technique of precise T_2 extraction, rather a fast and simple method of obtaining a reliable estimate.

6 Conclusion

In this thesis the historically first multi-frequency rapid-scan EPR experiments in THz frequency range and subsequent data processing are reported. Rapid-scan in general is a regime where either the field or the frequency is quickly scanned over the spectrum. If the time of the scan (or "sweep") is short relative to the electron relaxation times of the paramagnetic species, the spectrum gets progressively distorted by transient effects (so called "wiggles"). These can be removed from the spectrum by post-processing to obtain a steady-state spectrum.

We chose to perform the frequency-swept (magnetic field constant, frequency rapidly scanned) rapid-scan over the field-swept for a number of reasons:

1. The speed of the scan ("sweep rate") can reach much higher values (our maximum sweep rate of 61 500 THz/s corresponds to roughly 349 kT/s, compared to 11.8 T/s reported by Yu[17])

2. There are no eddy currents caused by a fast-changing external magnetic field in the sample holder and other parts of the spectrometer since the magnetic field is kept constant.

3. There is no need for a resonant cavity, therefore the sample is not limited by size, especially at higher frequencies. Namely this makes the rather easy implementation of multi-frequency experiments possible.

4. It is much easier to control the temperature of the sample while no scanning coil producing excess heat is used. This allows for measurement at low temperatures.

Additionally, frequency-swept rapid-scan EPR has only been done so far at frequencies below 100 GHz. Moving the research above this line is highly desirable because of several applications, including the DNP research and determination of relaxation times of thin film materials and oriented crystals at high fields and frequencies.

In the theoretical part of this thesis, we present basic knowledge of EPR principles and mechanisms necessary to understand our further work on the rapid-scan regime. That part includes the general principles, such as the resonance phenomenon, spin Hamiltonian for EPR purposes and mechanisms of electron spin ensemble relaxation. Additionally, we briefly discussed the linewidths of EPR spectra and general principles of CW and pulsed regimes.

The next chapter deals exclusively with the rapid-scan regime. First we introduced the historical background up to our research. Then we built the theoretical description of rapid-scan phenomenon by modifying the famous Bloch equations to suit the purpose; by those means we arrived at analytical solution of the phenomenon. In the next part of that chapter we presented a working theoretical model of extracting the steady-state solution from the rapid-scan spectrum by means of Fourier deconvolution.

The experimental part of the thesis deals with the description of the multi-frequency HFEPR spectrometer, which was slightly modified from its usual setup to accommodate

the rapid-scan experimental requirements, as is stated in the second part of that chapter, together with the description of the experimental procedure and samples.

We reported rapid-scan spectra of LiPc and BDPA samples measured at various field/frequency combinations. The progressive distortion with increasing the frequency sweep rate precisely matches theory and previous research. These two organic radicals were chosen due to them giving out a strong-signal, narrow, single spectral line, thus making them extremely simple to analyse. Since this thesis is not aimed at chemical analysis of the samples but rather the description of the rapid-scan experiment and data evaluation, these samples proved to be the perfect candidates. We used sinusoidal frequency modulation since we were able to achieve higher sweep rates than with an arbitrary waveform generator producing triangular sweeps.

We hand-picked the spectral areas to be 6.77 T / 190.4 GHz and 8.00 T / 225.0 GHz for the LiPc sample; 7.28 T / 204.4 GHz and 8.10 T / 227.4 GHz for the BDPA sample. These frequency spectral ranges were hand-picked since the signal in these areas was considerably stronger and more stable than in other areas (due to the standing waves in the optical path of the spectrometer). Maximum sweep rate of 61 500 THz/s (corresponding to roughly 349 kT/s) was employed for measuring these particular spectra. This proves our ability to conduct historically first multi-frequency rapid-scan experiments. All measurements were conducted at 13 K and averaged 4096 times.

In the next section we implement the theory stated in previous chapters into a home-written algorithm designed to extract the steady-state spectrum out of the rapid-scan measurements. By means of discrete Fourier Transform we were able to separate the excitation and the response of the system. For this we had to approximate the center of the sinusoidal sweep as being linear since we constructed the excitation function analytically as complex exponential with linear increase of frequency (corresponding to a real linear frequency sweep). Using this algorithm we were able to extract the steady-state spectrum from the rapid-scan one for every single one measurement that had been conducted; a few of them are reported in this thesis. It is obvious from comparison of the slow-scan spectra and the deconvoluted rapid-scan spectra that they match very well, although not quite perfectly – this is caused by approximating the sinusoidal sweep with a linear one in its center.

We were then able to obtain a reasonable estimation of the samples' spin-spin relaxation time T_2. This was done by numerically solving Bloch equations with rapid frequency sweeps in MATLAB (using the native function *ode45*) with variable T_2, which was manually adjusted until a sufficient similarity of the calculated and measured spectra was achieved. The resulting values were $T_2 = (50 \pm 10)$ ns for the BDPA sample and $T_2 = (12 \pm 2)$ ns for the LiPc sample. This is three orders of magnitude less for LiPc than reported in rapid-scan research of Stoner[37] at 250 MHz; the reported value being 2.5 µs. BDPA relaxation times were researched by Meyer[43] at X-band, the resulting value being 6.4 µs. Although relaxation times strongly depend on molecular environment and spectral range, thus the difference in results is not surprising. Additionally, to our best knowledge, no research on relaxation times in high frequencies has been published.

However, we were not able to separate the absorption and dispersion signals since we employed only one-channel detection. That lead to distortion of some of the absorption spectra that we were not able to address. In the future we plan to extend the experimental

setup to be able to use phase-sensitive detection to separate the absorption and dispersion signals. It is also worth mentioning that this thesis is but the first step in a valuable upcoming research and by no means presents highly refined and polished techniques and results; rather it should serve as a pointer to the power and possibilities of rapid-scan EPR.

This is historically the very first multi-frequency rapid-scan research capable to produce results at high fields and high frequencies. There is no resonant cavity needed for the experiment here, thus the flexibility of the offset frequency choice is enormous. The research reported in this thesis constitutes the next step in advancing the development of the invaluable rapid-scan EPR technique.

The biggest contribution of this research is the possibility to advance the offset frequencies of future rapid-scan measurements up to the Terahertz range. A simple exchange of the zero-bias detector allows us to conduct experiments at higher frequencies, thus we are able to examine DNP agents at relevant frequencies (263, 329 and 394 GHz); that is but one possible application. Others may include an improvement in the S/N ratio[18,19] and detection limit of quantitative EPR.[20]

The results of the research reported here are awaiting publication (O. Laguta, M. Tuček, J. van Slageren and P. Neugebauer. Multi-frequency rapid-scan EPR, manuscript in preparation).

References

[1] J.A. Weil and J.R. Bolton. *Electron Paramagnetic Resonance*. John Wiley & Sons, Inc., 2007.

[2] O. Stern and W. Gerlach. Der experimentelle Nachweis der Richtungsquantelung im Magnetfeld. *Zeitschrift für Physik*, 1:349–352, 1922.

[3] G.E. Uhlenbeck and S.A. Goudsmit. Ersetzung der Hypothese vom unmechanischen Zwang durch eine Forderung bezüglich des inneren Verhaltens jedes einzelnen Elektrons. *Die Naturwissenschaften*, 47:953–954, 1925.

[4] G. Breit and I.I. Rabi. Measurement of Nuclear Spin. *Phys. Rev.*, 11:2082–2083, 1931.

[5] I.I. Rabi, J.R. Zacharias, S. Millman, and P. Kusch. A New Method of Measuring Nuclear Magnetic Moment. *Phys. Rev.*, 4:318–318, 1938.

[6] E. Zavoisky. Spin-magnetic resonance in paramagnetics. *Fizichenskiĭ Zhurnal*, 9: 211–245, 1945.

[7] J. Frenkel. Viscous flow of crystalline bodies under the action of surface tension. *J. Phys. U.S.S.R.*, 9:385–391, 1945.

[8] J.I. Kaplan. Systems limitations on Fourier-Transform relationship between NMR free induction decay and CW line shape. *J. Chem. Phys.*, 57:5615–5616, 1972.

[9] J.I. Kaplan. Systems limitations on Fourier-Transform relationship between NMR free induction decay and CW line shape, a reply. *J. Chem. Phys.*, 59:990, 1973.

[10] J. Dadok and R. F. Sprecher. Correlation NMR spectroscopy. *J. Magn. Reson.*, 13: 243–248, 1974.

[11] R. K. Gupta, J. A. Ferretti, and E. D. Becker. Rapid scan Fourier Transform NMR spectroscopy. *J. Magn. Reson.*, 13:275–290, 1974.

[12] J. Jen. Rapid scan fourier transform NMR and chemical exchange. *J. Magn. Reson.*, 45:257–269, 1981.

[13] J.P. Joshi, J.R. Ballard, G.A. Rinard, R.W. Quine, S.S. Eaton, and G.R. Eaton. Rapid-scan EPR with triangular scans and fourier deconvolution to recover the slow-scan spectrum. *J. Mag. Res.*, 175:44–51, 2005.

[14] R. Beeler, D. Roux, and G. Bene. Rapid-passage effects in electron spin resonance. *Phys. Rev.*, 102:295, 1956.

[15] M. Weger. Passage effects in paramagnetic resonance experiments. *Bell System Tech. J.*, 39:1013–1112, 1960.

[16] J. Hyde and R. A. Strangeway. W-band frequency-swept EPR. *J. Magn. Reson.*, 205:93–101, 2010.

[17] Z. Yu, T. Liu, H. Elajaili, G.A. Rinard, S.S. Eaton, and G.R. Eaton. Field-stepped direct detection electron paramagnetic resonance. *J. Magn. Reson.*, 258:58–64, 2015.

[18] D.G. Mitchell, G.M. Rosen, M. Tseitlin, B. Symmes, S.S. Eaton, and G.R. Eaton. Use of Rapid-Scan EPR to Improve Detection Sensitivity for Spin-Trapped Radicals. *Biophysical Journal*, 105:338–342, 2013.

[19] D.G. Mitchell, M. Tseitlin, R.W. Quine, V. Meyer, M.E. Newton, and A. Schnegg. X-band rapid-scan EPR of samples with long electron spin relaxation times: a comparison of continuous wave, pulse and rapid-scan EPR. *Molecular Physics*, 111: 2664–2673, 2017.

[20] J. Möser, K. Lips, M. Tseitlin, G.R. Eaton, S.S. Eaton, and A. Schnegg. Using rapid-scan EPR to improve the detection limit of quantitative EPR by more than one order of magnitude. *J. Magn. Reson.*, 281:17–25, 2017.

[21] A. Abragam and M. Goldman. Principles of dynamic nuclear polarisation. *Rep. Prog. Phys.*, 41:395, 1978.

[22] A.W. Overhauser. Polarization of Nuclei in Metals. *Phys. Rev.*, 92:411, 1953.

[23] P. Neugebauer, D. Bloos, R. Marx, P. Lutz, M. Kern, and J. van Slageren. Ultra-broadband EPR spectroscopy in field and frequency domains. *PCCP*, 2018 accepted manuscript.

[24] L. Lumata, S.J. Ratnakar, A. Jindal, and Z. Kovacs. BDPA: An Efficient POlarizing Agent for Fast Dissolution Dynamic Nuclear Polarization NMR Spectroscopy. *Chem. Eur. J.*, 17:10825–10827, 2011.

[25] O. Haze, B. Corzilius, A. Smith, R.G. Griffin, and T.M. Swager. Water-Soluble Narrow-Line Radicals for Dynamic Nuclear Polarization. *J. Am. Chem. Soc.*, 134: 14287–14290, 2012.

[26] O. Laguta. *Magneto-optical investigations of Bismuth-doped silica glasses.* Doctoral thesis, Université de Lille 1-Science et Technologies, 2016.

[27] J.-M. Spaeth, J.N. Niklas, and R.H. Bartram. *Structural Analysis of Point Defects in Solids.* Springer-Verlag, 1992.

[28] S. Stoll and A. Schweiger. EasySpin, a comprehensive software package for spectral simulation and analysis in EPR. *J. Magn. Reson.*, 178:42–55, 2006.

[29] C. B. P. Finn, R. Orbach, and W. P. Wolf. Spin-lattice relaxation in cerium magnesium nitrate at liquid helium temperature - a new process. *Proc. Phys. Soc. (London)*, 77:261, 1961.

[30] R. Orbach. On theory of spin-lattice relaxation in paramagnetic salts. *Proc. Roy. Soc. (London)*, 77:821, 1961.

[31] J.H. Freed. On the Theory of Spin Relaxation of Gas Molecules: The Strong-Collision Limit. *J. Chem. Phys.*, 41:7–13, 1964.

[32] F. Bloch. Nuclear induction. *Phys. Rev.*, 70:460–474, 1946.

[33] A. Abragam and B. Bleaney. *Electron Paramagnetic Resonance of Transition Ions*. Oxford University Press, 1970.

[34] A. Schweiger and G. Jeschke. *Principles of Pulse Electron Paramagnetic Resonance*. Oxford University Press, 2001.

[35] P. Gast, D. Mance, E. Zurlo, K.L. Ivanov, M. Baldus, and M. Huber. A tailored multi-frequency EPR approach to accurately determine the magnetic resonance parameters of dynamic nuclear polarization agents: application to AMUPol. *PCCP*, 19:3777–3781, 2017.

[36] N. Bloembergen, E. M. Purcell, and R. V. Pound. Relaxation effects in nuclear magnetic resonance absorption. *Phys. Rev.*, 73:679–712, 1948.

[37] J.W. Stoner, D. Szymanski, Eaton. S.S., R.W. Quine, G.A. Rinard, and G.R. Eaton. Direct-detected rapid-scan EPR at 250 MHz. *J. Magn. Reson.*, 170:127–135, 2004.

[38] J.P. Joshi, G.R. Eaton, and S.S. Eaton. Impact of Resonator in Direct-Detected Rapid-Scan EPR at 9.8 GHz. *Appl. Magn. Reson.*, 28:239–249, 2005.

[39] M. Tseitlin, Z. Yu, R.W. Quine, G.A. Rinard, S.S. Eaton, and G.R. Eaton. Digitally generated excitation and near-baseband quadrature detection of rapid scan EPR signals. *J. Magn. Reson.*, 249:126–134, 2014.

[40] Z. Yu, R.W. Quine, G.A. Rinard, M. Tseitlin, H. Elajaili, V. Kathirvelu, L.J. Clouston, P.J. Boratynski, A. Rajca, R. Stein, H. Mchaourab, S.S. Eaton, and G.R. Eaton. Rapid-scan EPR of immobilized nitroxides. *J. Magn. Reson.*, 247:67–71, 2014.

[41] B. A. Jacobsohn and R. K. Wangsness. Shape of nuclear induction signals. *Phys. Rev.*, 73:942–946, 1948.

[42] K. Mobius, A. Savitsky, A. Schnegg, M. Plato, and M. Fuchs. Combining high-field EPR with site-directed spin labeling reveals unique information on proteins in action. *Magn. Reson. in Chem.*, 43:S4–S19, 2005.

[43] V. Meyer, Eaton. S.S., and G.R. Eaton. X-band Electron Spin Relaxation Times for Four Aromatic Radicals in Fluid Solution and Comparison with Other Organic Radicals. *Appl. Magn. Reson.*, 45:993–1007, 2014.

List of abbreviations

BDPA	α,γ-Bisdyphenylene-β-phenylallyl
CW	continuous wave
DNP	Dynamic Nuclear Polarization
EPR	Electron Paramagnetic Resonance
EZI	Electron Zeeman interaction
FDMR	Frequency-Domain Paramagnetic Resonance
FID	Free Induction Decay
FSI	Fine structure interaction
FT	Fourier Transform
HFEPR	High-Field Electron Paramagnetic Resonance
HFI	Hyperfine interaction
LiPc	Lithium Phthalocyanine
NMR	Nuclear Magnetic Resonance
NZI	Nuclear Zeeman interaction
QI	Quadrupole interaction
S/N	signal-to-noise
VCO	voltage controlled oscillator
VTI	variable temperature insert